12-2018

Synthesis, Characterization, and Catalytic Activity of Copper Palladium Oxide Solid Solutions.

Gregory L. Christensen
University of Nebraska-Lincoln, gcutah@huskers.unl.edu

Synthesis, Characterization, and Catalytic Activity of Copper Palladium Oxide Solid Solutions.

by

Gregory L. Christensen

A Thesis

Presented to the Faculty of

The Graduate College at the University of Nebraska

In Partial Fulfillment of Requirements

For the Degree of Master of Science

Major: Chemistry

Under the Supervision of Professor Marjorie A. Langell

Lincoln, Nebraska

December, 2018

Synthesis, Characterization, and Catalytic Activity of Copper Palladium Oxide Solid Solutions.

Gregory Christensen M.S.

University of Nebraska, 2018

Advisor: Marjorie A. Langell

$Cu_xPd_{1-x}O$ forms a homogeneous solid solution over the wide range of $0 \leq x \leq 0.725$ in which compositional variation can be correlated with structural and chemical environmental changes. After a small lag at low Cu^{2+} concentrations, where the lattice cell parameters are pinned to that of the pure PdO structure, $Cu_xPd_{1-x}O$ lattice parameters follow Vegard's law in which the cell volume decreases linearly with x, indicating a homogenous solution in which Cu^{2+} randomly replaces the larger Pd^{2+} cation. The crystal structure also undergoes an increase in the c/a cell ratio, which relaxes the tetragonal distortion around the metal cation and shifts the metal-oxygen distance towards that of pure CuO (tenorite). X-ray photoelectron spectroscopy (XPS) shows a linear increase in Pd^{2+} 3d and Cu^{2+} 2p binding energies with increased Cu^{2+}, a result of the increased Madelung energy and relaxation effects which occur during the photoemission process. XPS and Auger Electron Spectroscopy (AES) indicate that the surface composition is comparable to that of the bulk, and copper XPS Auger parameter analysis confirms a different, and variable, environment for copper in $Cu_xPd_{1-x}O$ than is found in pure tenorite.

Solid solutions of $Cu_xPd_{1-x}O$ have been prepared with x values of 0, 0.2, 0.4, 0.6, and 1 for use as catalysts in the dehydrogenation of isopropanol to form acetone. Solid solution catalysts were shown to be less efficient catalysts when compared to mixtures of

equal atomic composition. SEM images were obtained and showed morphology changes after heating of the samples. Surface area of the catalysts was determined by BET. UV/VIS was used to determine reactant and product concentrations. XPS data were obtained on the catalysts before and after the reactions, showing reduction of the catalyst occurred during catalysis.

Table of Contents

List of Figures

List of Tables

Acknowledgements

I am grateful to my advisor Dr. Langell for her guidance and patience. She has taught me much about science and research. I am thankful to have been able to learn about and use XPS systems in my research. I am thankful to my wife for letting me hide in the office for so many hours in order to complete my work. I thankful to my kids who were born during my time of study and have been a source of happiness and a way to clear my mind at times. I would like to thank my graduate committee members for their time and effort to help me. I am thankful to the many professors that have mentored me through the classes they taught, being available for office hours, and for being able to work as a teaching assistant for them.

Chapter One: Introduction

I. A. Purpose of Study

The purpose of this study is to examine the physical and catalytic properties of the CuxPd1-xO solid solution series up to the limit of solubility. Copper oxide and palladium oxide were chosen because they both show promise as catalysts and it is known that CuO has a high solubility in PdO[1]. While they do not have the same lattice structure, the structures do have some similarities in metal coordination and metal-oxygen bonding, and copper cations will dissolve into the palladium oxide and take on its parent lattice structure. X-ray diffraction (XRD) data will be used to show that as the copper concentration increases, the palladium oxide lattice constants decrease to accommodate a smaller ionic radius. X-ray photoelectron spectroscopy (XPS) and Auger electron spectroscopy (AES) will be used to compare the surface composition of the samples to that of the as prepared bulk composition. BET surface area measurements were performed on select solid solution samples and compared to non-solid solution mixtures of equal composition. Scanning electron microscope images were taken of select samples to better understand surface morphology. Solid solution samples and non-solid solution samples were utilized as catalysts in the dehydrogenation of isopropanol to acetone.

I. B. PdO, CuO and $Cu_xPd_{1-x}O$ Systems

Transition metal oxides are often used as catalysts because they are able to serve as a source of oxygen, which can then be readily replenished to the surface under fairly mild reaction conditions. It is thought that PdO_x is the active phase of the Pd metal

catalysts such as in the Pd/Al_2O_3 supported catalytic systems[2]. For it to be catalytically active, studies suggest that PdO must have some oxygen defects which is indicated by writing PdO_x[3]. PdO is a fairly strong oxidation catalyst and is known to have high activity as a catalyst for methane combustion[4]. PdO has also been shown to catalyze such reactions as the photocatalytic bacteria inactivation[5,6], photocatalytic degradation of organic pollutants[7], and CO oxidation[8].

CuO is generally a milder catalyst than is PdO and is thus often employed in partial oxidation catalysis. CuO has been utilized as a catalyst in many processes such as methanol synthesis from CO_2 hydrogenation[9], steam reforming[10], the water-gas shift reaction[11,12,13,14,15], and NO_x decomposition[16]. CuO has also been shown to be more catalytically active than many other metal oxides in the oxidation of phenol and other alcohols to aldehydes [17]. When combined with co-catalysts such as CeO_2, CuO has been shown to have an increased activity in several catalysis reactions such as the oxidation of CO[18,19,20,21,22,23,24] and the steam reforming of ethanol and dry reforming of ethanol.[25]

CuO has many other uses, for example as in solar-absorbing selective coating in solar cells.[26] CuO is a p-type semiconductor[27] with a band gap of 1.2eV and has photoconductive properties.[28] In nanoparticle form, CuO has been shown to exhibit room temperature ferromagnetism[29]. CuO is also used in gas sensors[28], desulfurization sorbent[30,31], superhydrophobic surfaces[32], and even as a textile bactericide[33] and as an antimicrobial agent[34]. CuO may even have a place in lithium ion batteries as an anode material[35].

Palladium oxide and copper oxide, while both active in oxidation catalysis exhibit substantially different catalytic activity. Pd and Cu have been shown to have better

catalytic activity for the water gas shift reaction when the two metals were combined. It, therefore, might be beneficial to combine copper oxide with palladium oxide to produce a more active oxidation catalyst, and we propose that the effect will be more pronounced if the two are intimately mixed, as is found in the $Cu_xPd_{1-x}O$ solid solution. This system has the added benefit of having a substantial range of solubility[36] of $0 \leq x \leq 0.7$ leading to the possibility of tailoring the catalytic activity compositionally. In addition to enhanced catalytic activity, cost can also be a factor in choosing the solid solution over the pure oxide. PdO is expensive and CuO can be dissolved into PdO to reduce catalyst cost and maintain the PdO lattice structure. The $Cu_xPd_{1-x}O$ solid solution is proposed to have new or different catalytic activities from the individual components and it is hoped that by dissolving CuO into PdO that a cheaper/more efficient catalyst will be realized.

I. C. Copper and Palladium oxide Crystal Structure

PdO is a p-type semiconductor. In PdO, palladium is in the Pd^{2+} form, giving it an electronic configuration of $1s^22s^22p^63s^23p^63d^{10}4s^24p^64d^8$, with the associated tendency to square planar coordination. This leaves two 5s and two 4d orbitals available for molecular interactions and participation in catalytic processes. Palladium oxide is found in a tetragonal crystal lattice structure as shown in figure 1.1. PdO has lattice parameters of a = b = 3.0434 Å and c = 5.3363 Å and a cell volume of 49.43 Å[37],[38],[39] The coordination in palladium oxide is approximately square-planar around Pd^{2+}, with four equidistant oxygen ions, and O^{2-} in tetrahedral coordination. A distortion relaxes the local symmetry around the palladium from a nominally D_{4h} point group, with equivalent Pd to O nearest neighbor bond lengths of 2.024 Å but with pairs of O−Pd−O angles of

82.5°/97.5°. CuO forms a monoclinic structure with lattice parameters of a = 4.6837 Å, b = 3.4226 Å, c = 5.1289 Å, and β = 99.54° and a cell volume of 82.23 Å[40],[41].

CuO is found as the mineral tenorite and has a monoclinic lattice structure as seen in figure 1.2. The lattice belongs to the C2/c space group. Copper is also formally Cu^{2+} and the ion has a $1s^2 2s^2 2p^6 3s^2 3p^6 3d^9$ electronic configuration leaving two 4s orbitals and one 3d orbital unoccupied and available for molecular interactions or participation in catalytic processes. CuO nominally places Cu^{2+} in 6-fold coordination; however, the structure is severely distorted from an ideal octahedron. As in PdO, Cu^{2+} is also surrounded by four O^{2-} in approximate square-planar coordination at ~ 2 Å but has two more distant apical O^{2-} ions. The formal configuration of $[Ar]3d^9$ makes the Cu^{2+} ion an ideal candidate for Jahn−Teller distortion due to the odd number of electrons in the d-orbital, and the two apical Cu to O bond distances are elongated by about 42%, at 2.784 Å, relative to the planar Cu to O nearest-neighbor bonds found at 1.956−1.958 Å. The PdO structure can be envisioned as an extreme form of Jahn-Teller distortion in which the apical oxygens are removed to infinity. Thus, a solid solution of Cu dissolved into the PdO lattice should produce copper in a very different environment than that found in its native tenorite.

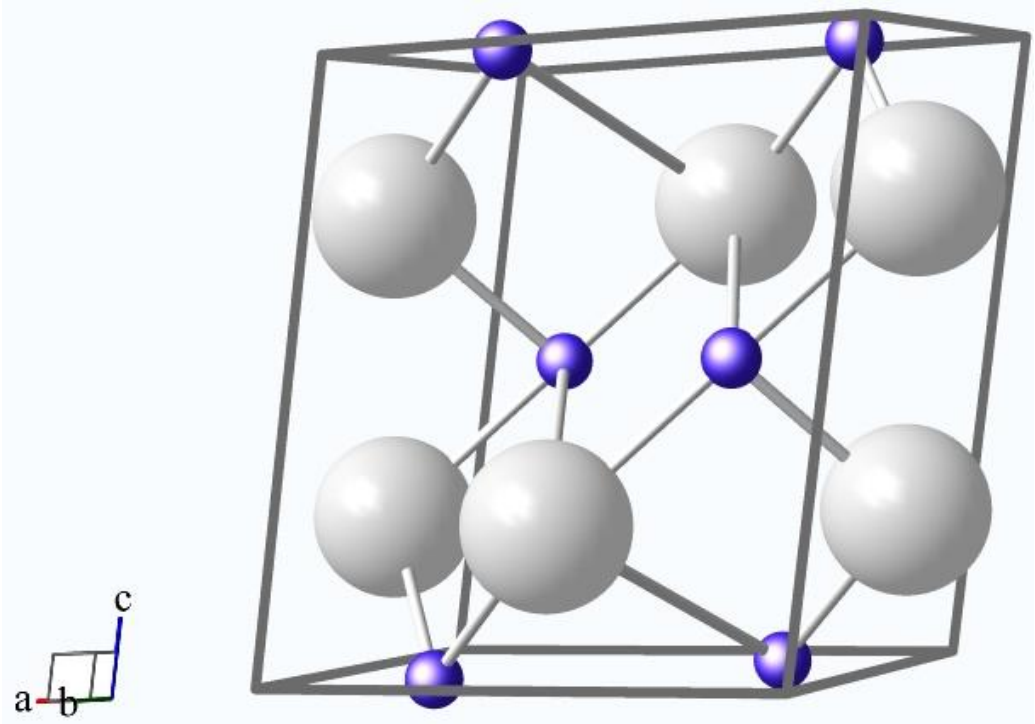

Figure 1.1 Copper Oxide Lattice Structure. Copper ions are blue and oxygen ions are white.

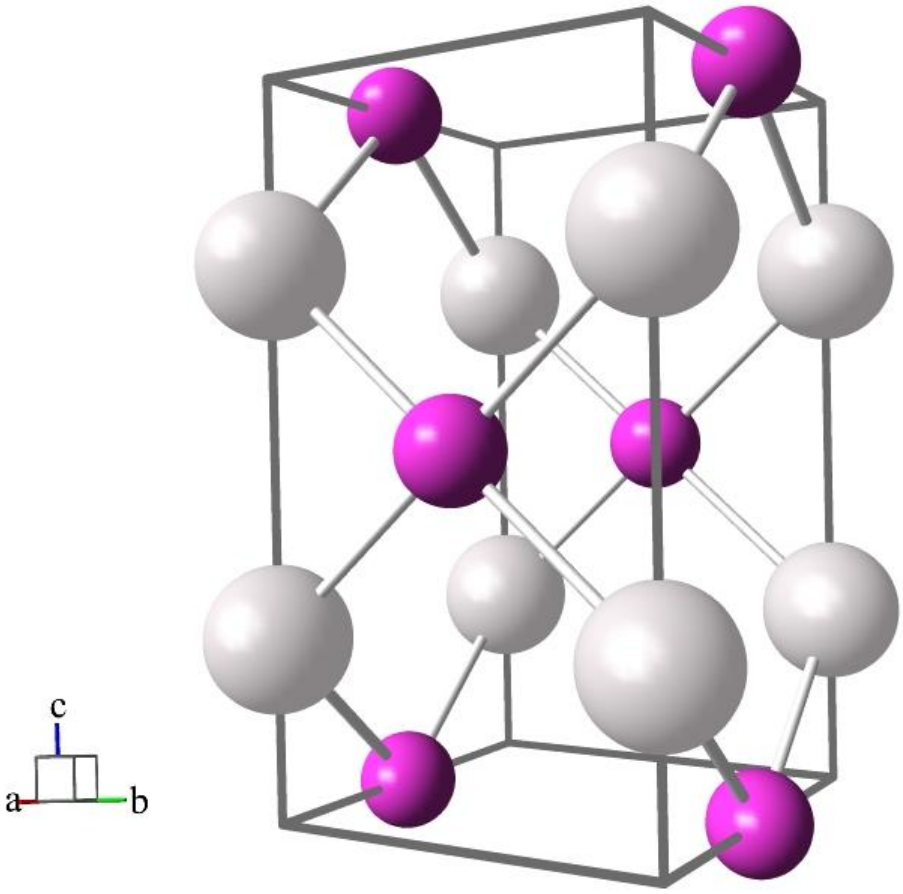

Figure 1.2 Palladium Oxide Lattice Structure. Palladium ions are represented by the pink/purple spheres and oxygen by the white spheres.

I. D. Solid solutions

Solid solutions are formed when a solute atom is placed into a solvent crystal lattice without changing the solvent crystal structure. Solid solutions can contain interstitial or substitutional atoms. Interstitial solid solutions have solute atoms placed in between atoms normally occupied in the crystal lattice. Substitutional atoms exist when a lattice atom is replaced by a solute atom. In each case, the original crystal lattice structure is maintained, but the lattice parameters can be affected by the addition of the solute atoms. There are some general guidelines that can be used to help determine

whether a solid solution will form and a rule of thumb is that for substitutional solid solutions the size of the solute atoms should be similar to that of the solvent atoms and of equal oxidation state.

Vegard's law[42,43,44,45] is an empirical observation that the unit lattice cell parameters vary linearly with solute concentration to accommodate the different size of the solute cation relative to the solvent cation. According to Vegard's law, substitution of smaller solute ions into a crystal lattice structure decreases the lattice constants linearly as the smaller ion concentration increases up to the point of phase separation. Vegard's law only applies to substitutional solid solutions and not interstitial atoms in which a small atom such as hydrogen may fit in between lattice atoms without changing the lattice constants significantly while maintaining the original crystal lattice structure.

The solid solution forms because entropy drives it. The entropy of mixing will overcome the increased lattice energy of the mixed metal oxide over that of the pure oxide. When entropy can no longer do this, phase separation occurs.

For an oxide solid solution to form in a reasonable timeframe, diffusion must generally be increased by heating the sample. In the case of the solid solution $Cu_xPd_{1-x}O$, the two separate CuO and PdO powders are mixed together very well and then pressed together in order to put the two materials as close as possible to minimize the necessary migration distance. Then sufficient energy in the form of heat is applied at just below the lowest melting point until a solid solution is formed. At sufficiently high temperatures, the atoms will have energy that the Cu^{2+} ions atoms will diffuse into the PdO lattice, allowing them to substitute for the Pd^{2+} cations. In the solid solution, when the smaller

Cu^{2+} (ionic radius r ≈ 0.57 Å) replaces the Pd^{2+} (r ≈ 0.64 Å) in the PdO lattice the $Cu_xPd_{1-x}O$ lattice constants will decrease.

I. E. Conclusion

Both CuO and PdO are useful catalysts. The ability of Cu^{2+} to dissolve into the PdO lattice structure at high concentrations allows for a wide compositional range to tailor a catalyst for specific properties. A solid solution of $Cu_xPd_{1-x}O$ is able to maintain the PdO lattice structure over a substantial range of solubility up to about 72.5 mol% and unit cell constants decrease according to Vegard's law as the CuO concentration is increased[46]. The solid solution does not show improved catalytic activity over the simple mixture samples; it could be that the oxidation of isopropanol is not as efficient by PdO and the catalytic reaction is dominated by single-site surface atoms.

References

[1] Schmahl, N. G., Eikerling, G. F., Über Kryptomodifikationen des Cu(II)-Oxids, Zeitschrift für Physikalische Chemie Neue Folge, **1968** Bd. 62, S. 268-279.

[2] Dianat, A., Seriani, N., Bobeth, M., Pompe, W., Ciacchi, L. C., DFT Study of the Thermodynamic Stability of Pd-Pt Bulk Oxide Phases, J. Phys. Chem. C **2008**, 112, 13623-13628.

[3] Wang, S.Y., LI, N., Zhou, R. M., Jin, L. Y., Hu, G. S., Lu, J. Q., Luo, M. F., Comparing the CO Oxidation Activity of Free PdO and Pd^{2+} ions over PdO-CeO_2/SiO_2 Catalysts, Journal of Molecular Catalysis A, **2013**, (374-375), 53-58.

[4] Rogal, J., Reuter, K., Scheffler, M., Thermodynamic Stability of PdO Surfaces, Physical Review B **2004**, 69, 075421.

[5] Wu, Pi., Xie, R., Imlay, K., Shang, J. K., Monolithic Ceramic Foams For Ultrafast Photocatalytic Inactivation of Bacteria, J. Am. Ceram. Soc. **2009**, 92 (8), 1648-1654

[6] Li, Q., Li, Y. W., Liu, Z., Xie, R., Shang, J. K, Memory Antibacterial Effect From Photoelectron Transfer Between Nanoparticles and Visible Light Photocatalyst, J. Mater. Chem., **2010**, 20, 1068-1072.

[7] Li, Q., Shang, J. K., Composite Photocatalyst of Nitrogen and Fluorine Codoped Titanium Oxide Nanotube Arrays With Dispersed Palladium Oxide Nanoparticles for Enhanced Visible Light Photocatalytic Performance, Environ. Sci. Technol. **2010**, 44, 3493-3499.

[8] Zorn, K., Giorgio, S., Halwax, E., Henry, C. R., Grönbeck, H., Rupprechter, G., J. Phys. Chem. C **2011**, 115, 1103-1111.

[9] Guo, X., Mao, D., Lu, G., Wang, S., Wu, G., Glycine-nitrate combustion synthesis of CuO-ZnO-ZrO_2 catalyst for methanol synthesis from CO_2 hydrogenation, Journal of Catalysis, **2010**, 271(2), 178-185.

[10] Huang, G., Liaw, B. J., Jhang, C. J., Chen, Y. Z., Steam Reforming of Methanol Over CuO/ZnO/CeO_2/ZrO_2/Al_2O_3 Catalysts, Applied Catalysis A: General **2009,** 358, 7-12.

[11] Budhi, Y. W., Putri, D. D., Husna, A., Irawan, H. K., Miyamoto, M., Uemiya, S., Dynamic operation of water gas shift reaction over Fe_2O_3/Cr_2O_3/CuO catalyst in Pd/Al_2O_3 membrane reactor , **2018**, *IOP Conf. Ser.: Earth Environ. Sci.* 105**,** 012020.

[12] Zhang, Z., Wang, S. S., Song, R., Cao, T., Luo, L., Chen, X., Gao, Y., Lu, J., Li, W. X., Huang, W., The Most Active Cu Facet for Low-Temperature Water Gas Shift Reaction, Nature Communications, **2017**, 8(488) 1-10.

[13] Ayastuy, J. L., Ortiz, M. A. G., Marcos, J. A. G., Aranzabal, A., Velasco, J. R. G., Kinetics of the Low-Temperature WGS Reaction over a CuO/ZnO/Al2O3 Catalyst, Ind. Eng. Chem. Res., **2005**, 44(1) 41-50.

[14] Li, L., Zhan, Y., Zheng, Q., Zheng, Y., Chen, C., She, Y., Lin, X., Wei, K., Water–Gas Shift Reaction over CuO/CeO_2 Catalysts: Effect of the Thermal Stability and Oxygen Vacancies of CeO_2 Supports Previously Prepared by Different Methods, Catalysis letters, **2009**, 130(3-4), 532-540.

[15] Zhang, Y., Chen, C., Lin, X., Li, D., Chen, X., Zhan, Y., Zheng, Q., CuO/ZrO_2 catalysts for water–gas shift reaction: Nature of catalytically active copper species, Int. Journal of Hydrogen Energy, **2014**, 39(6), 3746-3754.

[16] Bizreh, Y. W., Al-Hamoud, L., AL-Joubeh, M., A Study on the Catalytic Activity of New Catalysts for Removal of NOx, CH and CO emitted from car exhaust, Journal of the Association of Arab Universities for Basic and Applied Sciences, **2014**, 16, 55-63.

[17] Pande, S., Saha, A., Jana, S., Sarkar, S., Basu, M., Pradhan, M., Sinha, A. K., Saha, S., Pal, A., Pal, T., Resin-Immobilized CuO and Cu Nanocomposites for Alcohol Oxidation, Organic Letters, **2008,** 10 (22), 5179-5181.

[18] Luo, M. F., Song, Y. P., Lu, J. Q., Wang, X. Y., Pu, Z. Y., Identification of CuO Species in High Surface Area CuO-CeO_2 Catalysts and Their Catalytic Activities for CO oxidation, J. Phys. Chem. C **2007**, 111, 12686-12692.

[19] Arias, A. M., Garcia, M. F., Gálvez, O., Coronado, J. M., Anderson, J. A., Conesa, J. C., Soria, J., Munuera, G., Comparitive Study on Redox Properties and Catalytic Behavior for CO Oxidation of CuO/CeO_2 and CuO/$ZrCeO_4$ Catalysts, Journal of Catalysis, **2000,** 195 (1), 207-216.

[20] Avgouropoulos, G., Loannides, T., Selective CO Oxidation over CuO-CeO_2 Catalysts Prepared Via The Urea-Nitrate Combustion Method, **2003,** 244 (1), 155-167.

[21] Gamarra, D., Belver, C., Garcia, M. F., Arias, A. M., Selective CO Oxidation in Excess H_2 Over Copper-Ceria Catalysts: Identification of Active Entities/Species, Journal of the american chemical society, **2007**, 129 (40), 12064-12065.

[22] Rao, K. N., Bharali, P., Thrimurthulu, G., Reddy, B. M., Supported Copper-Ceria Catalysts for Low Temperature CO Oxidation, Catalysis Communications, **2010,** 11 (10), 863-866.

[23] Luo, M. F., Ma, J. M., Lu, J. Q., Song, Y. P., Wang, Y. J., High-Surface Area CuO-CeO_2 Catalysts Prepared by a Surface-Templated Method For Low-Temperature CO Oxidation, Journal of Catalysis, **2007,** 246 (1), 52-59 .

[24] Jia, A. P., Jiang, S. Y., Lu, J. Q., Luo, M. F., Study of Catalytic Activity at the CuO-CeO_2 Interface for CO Oxidation, J. Phys. Chem. C **2010**, 114, 21605-21610.

[25] Djinović, P., Batista, J., Ćehić, B., Pintar, A., Utilization of High Specific Surface Area CuO-CeO_2 Catalysts for High Temperature Processes of hydrogen Production: Steam Re-forming of Ethanol and Methane Dry Re-forming, J. Phys. Chem. A **2010**, 114, 3939-3949.

[26] Qunwu, H., Yiping, W., Jinhua, L., Preparation of Solar Selective Absorbing CuO Coating For Medium Temperature Application, Front. Chem. Eng. China **2007**, 1 (3), 256–260.

[27] Liu, J., Huang, X., Li, Y., Sulieman, K. M., He, X., Sun, F., Hierarchical Nanostructure of Cupric Oxide on a Copper Substrate: Controllable Morphology and Wettability, J. Mater. Chem., **2006**, 16, 4427-4434.

[28] Manna, S., Das, K., De, S. K., Template-Free Synthesis of Mesoporous CuO Dandelion Structures For Optoelectronic Applications, Applied Materials and Interfaces, **2010**, 2 (5), 1536-1542.

[29] Gao, D., Zhang, J., Zhu, J., Qi, J., Zang, Z., Sui, W., Shi, H., Xue, D., Vacancy-Mediated Magnetism in Pure Copper Oxide NanoParticles, Nanoscale Res Lett **2010,** 5, 769-772.

[30] Sasaoka, E., Hatori, M., Yoshimura, H., Su, C., Role of Desulfurization Sorbent Fe_2O_3 and CuO in the Presence of O_2, Ind. Eng. Chem. Res. **2001**, 40, 2512-2517.

[31] Jeong, S. M., Kim, S. D., Removal of NO_x and SO_2 by CuO/γ-Al_2O_3 Sorbent/Catalyst in a Fluidized-Bed Reactor, Ind. Chem. Res. **2000**, 39, 1911-1916.

[32] Li, J., Liu, X., Ye, Y., Zhou, H., Chen, J., Fabrication of Superhydrophobic CuO Surfaces with Tunable Water Adhesion, The Journal of Physical Chemistry C, **2011**, 115 (11), 4726-4729.

[33] Torres, A., Ruales, C., Pulgarin, C., Aimable, A., Bowen, P., Sarria, V., Kiwi, J., Innovative High-Surface-Area CuO Pretreated Cotton Effective in Bacterial Inactivation under Visible Light, Applied Materials & Interfaces, **2010**, 2 (9), 2547-2552.

[34] Ren, G., Hu, D., Cheng, E. W. C., Reus, M. A. V., Reip, P., Allaker, R. P., Characterisation of Copper Oxide Nanoparticles for Antimicrobial Applications, International Journal of Antimicrobial Agents **2009,** 33, 587-590.

[35] Yang, M., Gao, Q., Copper Oxide and Ordered Mesoporous Carbon Composite with High Performance using as Anode material for Lithium –Ion Battery, Microporous and Mesoporous Materials, **2011,** 143, 230-235.

[36] Schmahl, N. G., Eikerling, G. F., Über Kryptomodifikationen des Cu(II)-Oxids, Zeitschrift für Physikalische Chemie Neue Folge, **1968** Bd. 62, S. 268-279.

[37] Liu, J., Huang, X., Li, Y., Sulieman, K. M., He, X., Sun, F., Hierarchical Nanostructures of Cupric Oxide on a Copper Substrate: Controllable Morphology and Wettability. J. Mater. Chem. **2006**, 16 (45), 4427−4434.

[38] Rogers, D. B., Shannon, R. D., Gillson, J. L., Crystal Growth and Semiconductivity of Palladium Oxide. J. Solid State Chem. **1971**, 3 (2), 313−316.

[39] Park, K. T., Novikov, D. L., Gubanov, V. A., Freeman, A. J., Electronic Structure of Nobel-metal Monoxides: PdO, PtO and AgO. Phys. Rev. B **1994**, 49 (7), 4425−4431.

[40] Liu, J., Huang, X., Li, Y., Sulieman, K. M., He, X., Sun, F., Hierarchical Nanostructures of Cupric Oxide on a Copper Substrate: Controllable Morphology and Wettability. J. Mater. Chem. **2006**, 16 (45), 4427−4434.

[41] Wold, A., Dwight, K., Solid State Chemistry Synthesis, Structure, and Properties of Selected Oxides; Chapman & Hall: New York, **1993**; p 94.

[42] Denton, A. R., Ashcroft, N. W., Vegard's Law, Physical Review A, **1991**, 43(6)

[43] King, H. W., Quantitative size-factors for metallic solid solutions, Journal of materials science 1, **1966**, 79-90.

[44] Jacob, K. T., Raj, S., Rannesh, L., Vegard's law: A fundamental relation of an approximation, International Journal of Materials Research: **2007**, 98(9), 776-77.

[45] Zen, E., Validity of vegard's law, American Mineralogist **1956**, 41(5-6):523-524.

[46] Schmahl, N. G., Eikerling, G. F., Über Kryptomodifikationen des Cu(II)-Oxids, Zeitschrift für Physikalische Chemie Neue Folge, **1968** Bd. 62, S. 268-279.

Chapter 2: Experimental

II. A. X-Ray Diffraction

X-ray diffraction (XRD) is a technique in which a sample is irradiated by an x-ray source to determine crystal lattice spacings. The electron density associated with the elements in the sample causes the x-rays to be scattered and the periodic structure of the atoms creates a diffraction pattern that is imaged by the detector. Through the use of peak positions and Bragg's law[47,48] the diffraction pattern can be used to obtain lattice parameters of the sample and its crystal structure.

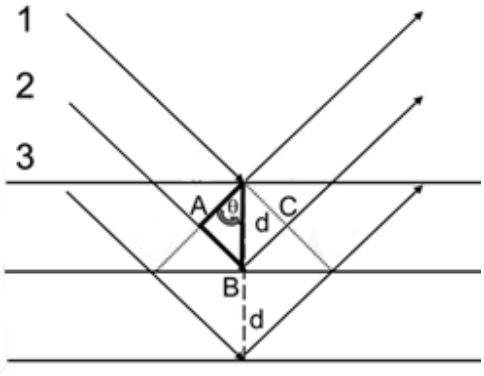

Figure 2.1 X-rays are diffracted with a pattern determined by interplanar spacings.

Bragg's law can be derived from figure 2.1 as set forth in the following steps. From figure 2.1 we see that:

$$\sin \theta = AB/d.$$

Where d is the interplanar spacing and θ is the diffraction angle equal to the angle of the incident beam. In order for the x-rays to be in phase, the extra distance (ABC) traveled by wave 2 compared to wave 1 must be an integer n multiplied by the wavelength (λ). Then $n \lambda = ABC = 2AB$ or $(1/2)n \lambda = AB$. This can be substituted in the previous equation to get Braggs law:

$$2d\sin\theta = n \lambda$$

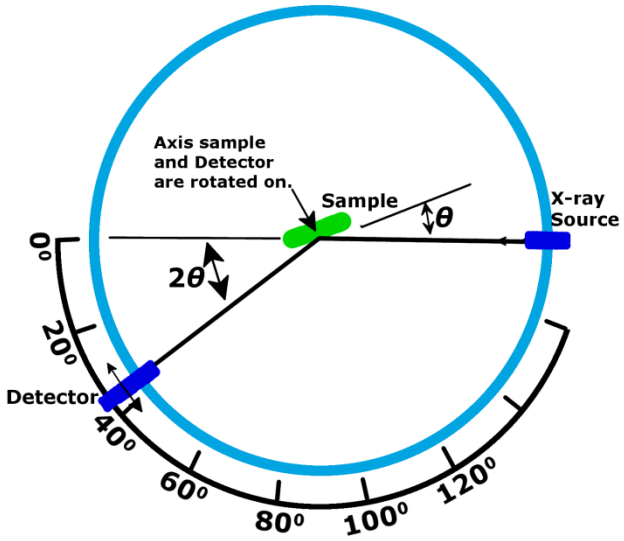

Figure 2.2 A typical X-ray diffraction setup containing the x-ray source, sample, detector, and axis sample and detector are rotated on.

Figure 2.2 is a typical X-ray diffraction setup, illustrating the incident angle θ relative to the surface plane and the detector angle 2θ relative to the incident X-ray beam. For this experiment, a copper X-ray source was used to produce Cu $k\alpha_{1,2}$ X-rays, at $k\alpha_1$ = 1.540562 Å and $k\alpha_2$ = 1.544390 Å. All samples were characterized by XRD using a Bruker-AXS D8 Discover diffractometer equipped with a General Area Detector Diffraction System (GADDS) area detector to confirm the phases present and to determine lattice parameters. Scans were taken in transmission mode over a 2θ range of 0−100° with a step size of 0.03°. A mirror exit slit size of 1.2 mm was used with pinhole slit size of 0.5 mm and a 0.5 mm snout. XRD analysis was performed using Topaz 2.1 software and since the source was not monochromatized, the data were fit with a $k\alpha_{1,2}$ lineshape in Rietveld analysis[49],[50].

II. B. Sample mounting and preparation for XRD

Samples were ground into a fine powder with a mortar and pestle to present a uniform distribution of crystal planes in the diffraction experiment and thus avoid

artifacts in relative diffraction peak intensities. The Bruker-AXS D8 utilizes a vacuum mount system and a convenient way to mount a sample for XRD analysis was to spread a thick layer of powder onto a one inch length of double-sided sticky tape that was previously attached to a glass slide. This allows the sample to cover a large area and gives a low noise, high peak intensity spectrum.

Figure 2.3 shows an XRD spectrum of palladium oxide and peak locations agree very well with accepted literature values[51,52,53,54,55,56]. The PdO XRD gives very low background noise and good peak intensity with the <101> showing the greatest intensity. In order to verify that no other structures are present, a 2θ range of 10 to 100^{o} was used.

Figure 2.4 is an XRD spectrum for $Cu_{0.50}Pd_{0.50}O$. The lattice pattern is that of the pure PdO lattice structure noted in figure 2.3 but with a noticeable peak shift observed due to the lattice contraction that occurs when smaller Cu^{2+} ions are substituted for the larger Pd^{2+} in the same crystal lattice structure. This phenomenon is described in greater detail in chapter 3 over a wide range of Cu^{2+} ions substituted in the PdO lattice structure.

Figure 2.5 contains an XRD pattern for pure copper oxide in the tenorite structure. The pattern is very different from that of the palladium oxide sample and also agrees very well with literature values[57,58,59,60]. CuO XRD has a low background with many peaks due to its lower monoclinic symmetry. CuO has many overlapping peaks as noted in the figure; for example, the peak at about 36^{o} contains both the <-111> and the <002> diffraction feature. This big difference between the XRD diffraction patterns of PdO and CuO allow for quick identification of the presence of either phase.

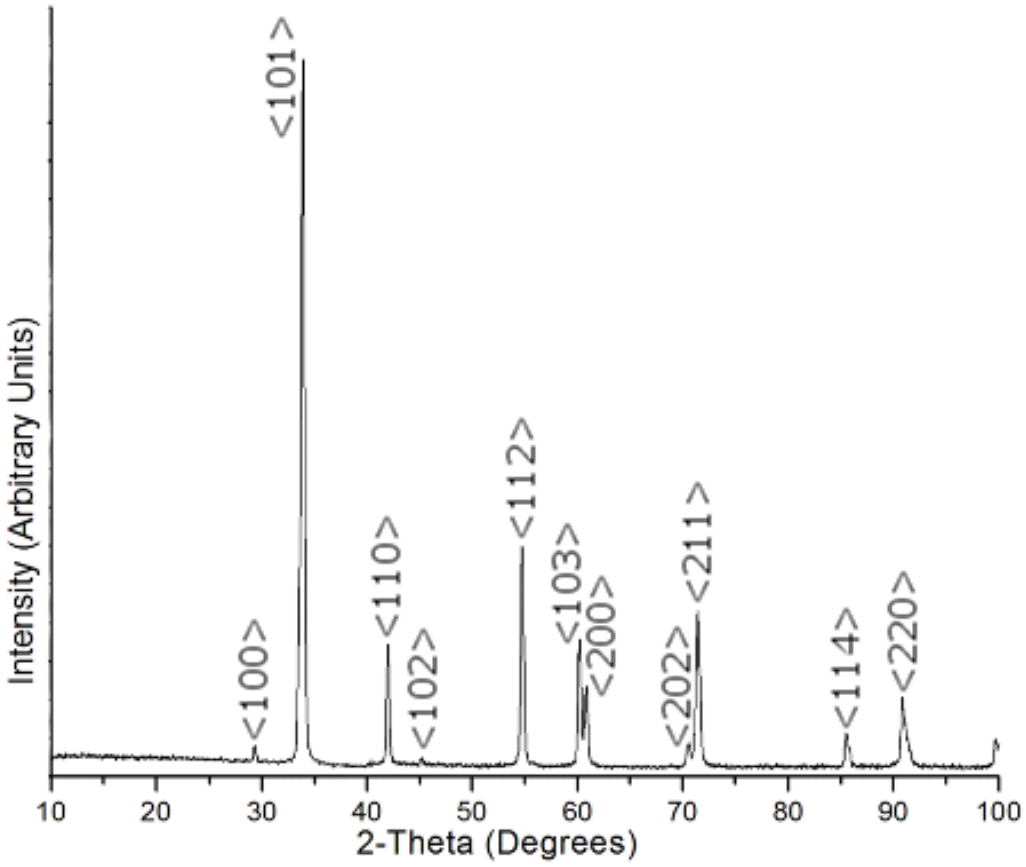

Figure 2.3 X-ray Diffraction pattern of PdO with labeled diffraction planes.

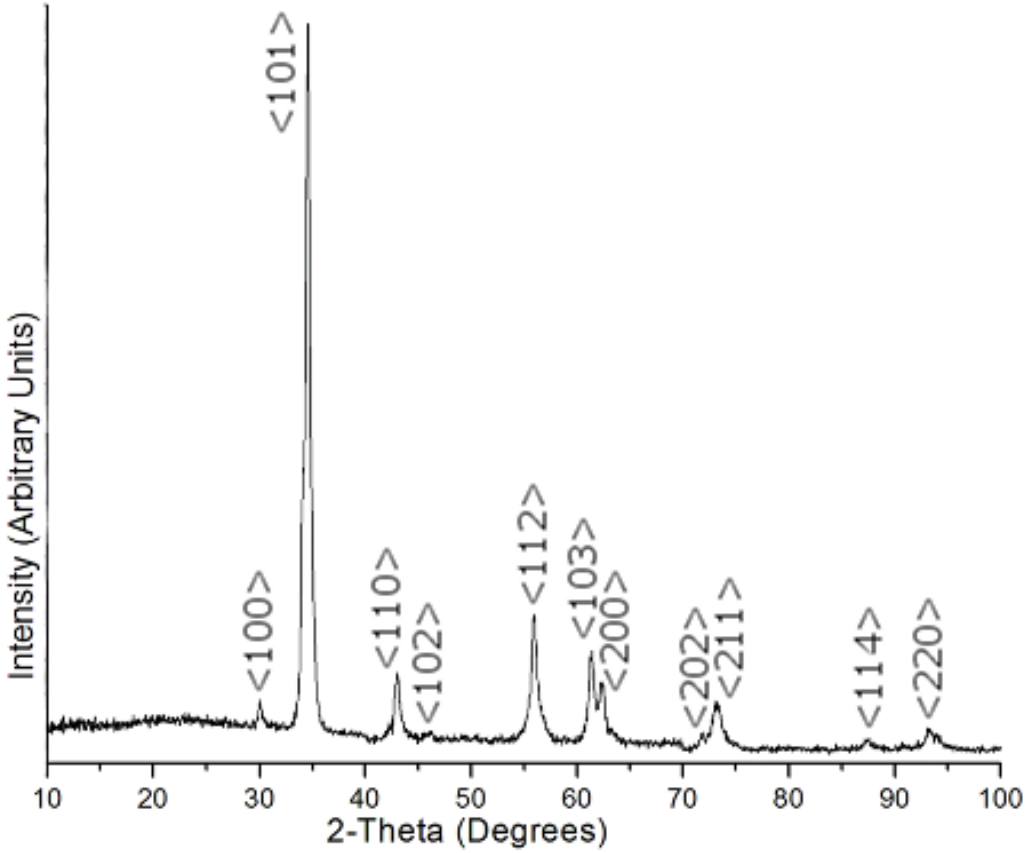

Figure 2.4 X-ray Diffraction pattern of $Cu_{0.50}Pd_{0.50}O$ with labeled diffraction planes.

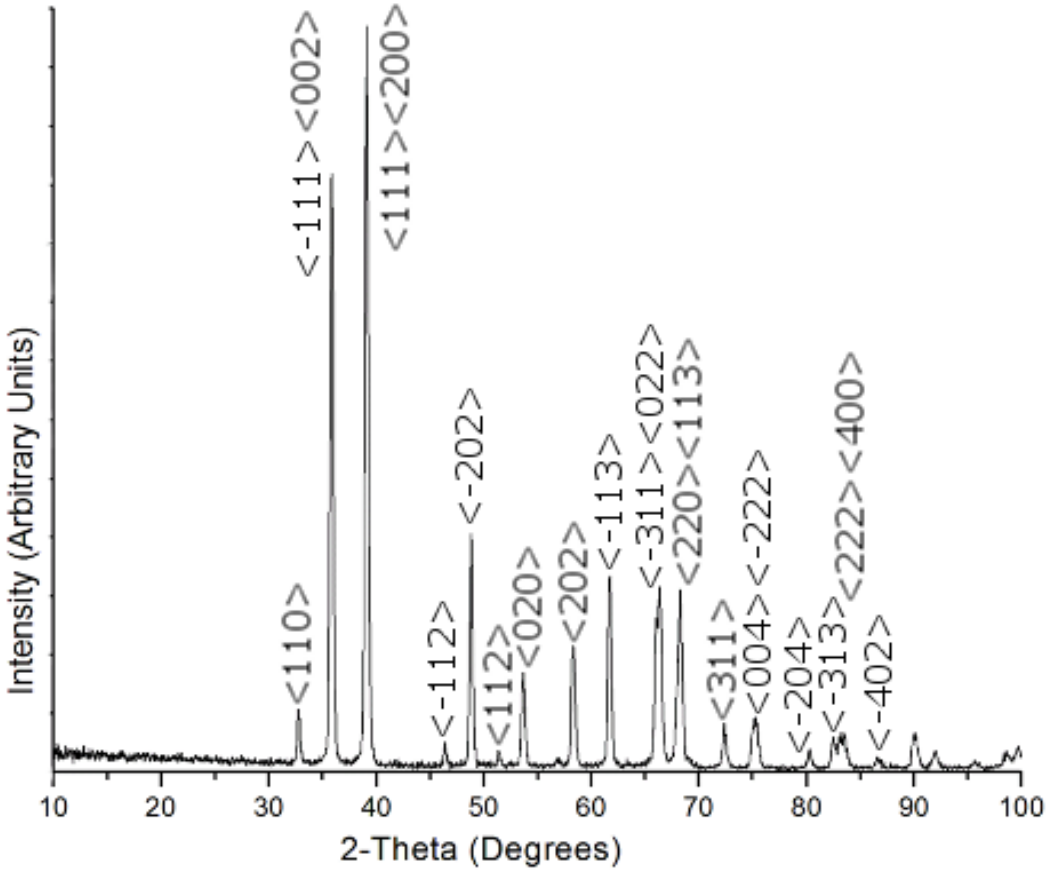

Figure 2.5 X-ray Diffraction pattern of CuO.

II.C. X-Ray Photoelectron Spectroscopy

X-Ray Photoelectron Spectroscopy (XPS) is a surface-sensitive technique in which a sample is placed in ultra-high vacuum and is irradiated with soft X-rays., This, in turn, excites electrons sufficiently that they are photoejected and travel towards an electrostatic analyzer that measures their kinetic energy and directs them through a slit and onto an electron multiplier for detection. A plot can then be produced with intensity vs. kinetic energy. It is customary however to use the label of binding energies (B.E.) instead of kinetic energies (K.E.).

$$B.E. = h\upsilon - K.E. - \phi$$

where ϕ is the work function of the spectrometer and $h\upsilon$ is the energy of the X-ray photons. XPS can be used to determine not only which atoms are present in the sample, but also their chemical environment, or oxidation state. The surface sensitivity of the XPS method ranges from 3-10nm, depending on the kinetic energy of the photoelectron. XPS can be used quantitatively to determine atomic concentrations of elements in the surface.

Figure 2.6 depicts a diagram for the XPS/AES chamber that was used for this research project. The sample is in powder form and is pressed into indium foil. The indium foil typically does not interfere with sample data collection and keeps other impurities out of the chamber that could be introduced by other sample holding methods such as tape. This foil, covered with the sample to be analyzed, is then placed in the center of a platen and secured with copper-beryllium "spoons" held in place with screws. The sample is loaded onto a magnetic rapid transfer arm that allows for the sample to be exchanged without venting the main chamber. Once the side arm is at a vacuum of 10^{-3} Torr or below the sample is placed in the main chamber and attached to the sample holder via a quick exchange mechanism. This quick exchange system works by turning the platen so that the prongs on the back side attach to its holder and then releases the front prongs that hold it to the transfer arm. The transfer arm may then be removed from the chamber. This process may increase the chamber pressure from 10^{-10} Torr to 10^{-8} Torr, but the ultra high vacuum quickly recovers to 10^{-9} Torr or below, low enough to begin acquiring data. Once the sample is loaded into the main chamber the sample tilt and rotation can be adjusted to maximize signal intensity. A sample is typically rotated to

place the surface normal parallel with the spectrometer detection angle and about 5^{o} relative to the spectrometer axis. The sample is electrically grounded to prevent charging which could occur for many metal oxide samples.

AES and XPS analyses were performed using a Physical Electronics (Φ) model 15-255G double pass cylindrical mirror analyzer in pulse count detection for XPS and in lock-in mode for AES with the analyzer driven by a Perkin Elmer Φ 11-055 ESCA/Auger system control. XPS photoemission was initiated with Al Kα radiation produced by a Φ 04-548 dual Mg/Al anode at 300 W and 15 kV using a Φ 14-040 X-ray generator. The XPS data were collected in 0.1 eV increments with a dwell time of 250 ms, and the spectra were signal averaged for 50− 200 scans depending upon the element and concentration. Pass energies of 50 eV were employed, unless otherwise noted. AES spectra were initiated with a 2 keV beam of electrons from a gun located concentric with the analyzer and controlled by a Φ Model 11-010 electron gun controller to produce a beam of 0.2 $\mu A/mm^2$. Data were obtained in the dN(E)/dE mode and were summed for five scans, each taken in 1 eV increments with a time constant of 0.1 s and a lock-in modulation energy of 5 eV. The XPS data were curve-resolved using XPS Peak 4.1 software.[61] A Shirley background[62,63] was used as a baseline for all peaks, and the data were curve-resolved using a 20% Lorentzian/80% Gaussian sum.

II. D. Sample mounting and preparation for XPS and AES analysis

Powder samples were freshly ground to produce a new surface prior to their admission into the ultrahigh-vacuum chamber by use of the rapid transfer admissions

system. The samples were mounted on clean indium foil for analysis and were measured by XPS and AES with no surface pretreatment or additional in situ UHV conditioning.

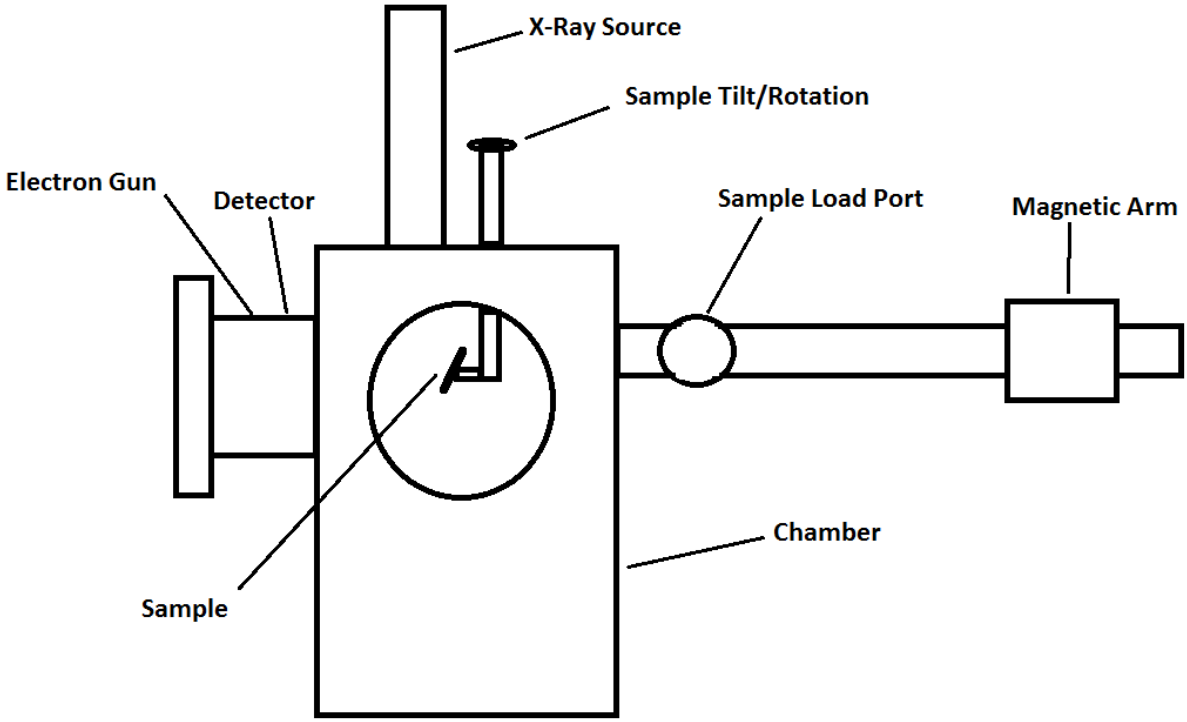

Figure 2.6 XPS/AES Chamber Setup.

Figure 2.7 shows an XPS broad scan of pure PdO powder with peaks labeled to indicate their origin. The background in the spectrum is created by photoelectrons that have lost energy due to inelastic scattering, which is also responsible for the asymmetric shape of the photoemission peak which tails to higher binding energy. The carbon peak is from carbon contamination of the sample that occurs over time from exposure to the air or from manipulation of the sample as it is being mounted on the indium foil, and is used as a reference peak[64]. The oxidation state of an atom can be determined by its binding energy and the atomic concentration can be calculated from the peak intensity ratios. Examples are written in chapter three. The O 1s peak is very near the Pd $3p_{3/2}$ peak and is resolved only upon taking a higher resolution scan as done in chapter three. The Auger

peaks are labeled according to nuclear physicists' nomenclature K, L, M, N. The letter K indicates a 1s shell electron or n = 1 shell. Subscripts indicate the orbital, where a 1 is for an s orbital (omitted for the K designation), 2,3 are for p orbitals, 4,5 are for d orbitals, and 6,7 are for f orbitals. The letter L denotes a n = 2 shell so L_1 is a 2s level, $L_{2,3}$ is a 2p level and with M representing n = 3, N representing n = 4, and O representing n = 5 shells. V is commonly used to denote a valence band. The Auger process is drawn out in figure 2.10. Auger label order is 1st ionized electron, decay electron, Auger Electron giving a three letter designation.

Figure 2.8 shows the XPS broad scan for a pure CuO sample with labeled peaks. It can be seen that there is good separation of the Cu $2p_{1/2}$ and the Cu $2p_{3/2}$ peaks as well as the O 1s peak. In figure 2.9 we see a broad scan of $Cu_{.05}Pd_{.95}O$. The peak intensity of Cu is much less than that of Pd due to the low Cu concentration of the selected sample. Relative peak intensity is proportional to the elemental concentration, discussed more extensively in chapter three.

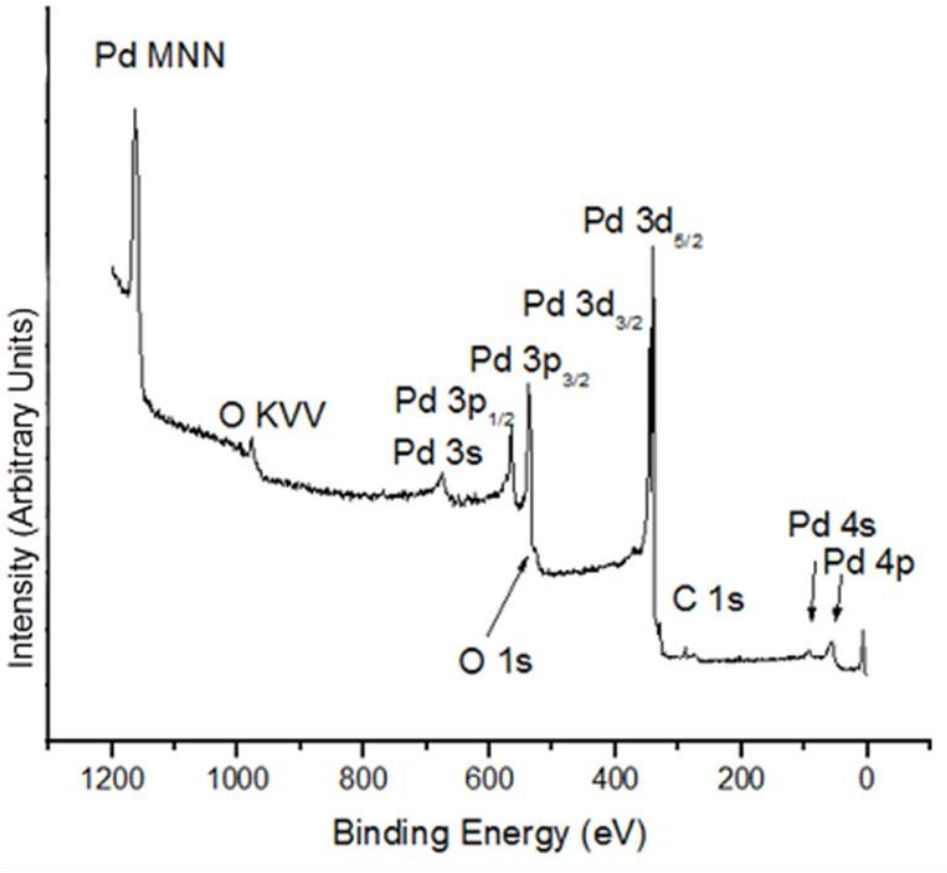

Figure 2.7 XPS broad scan of as purchased PdO powder.

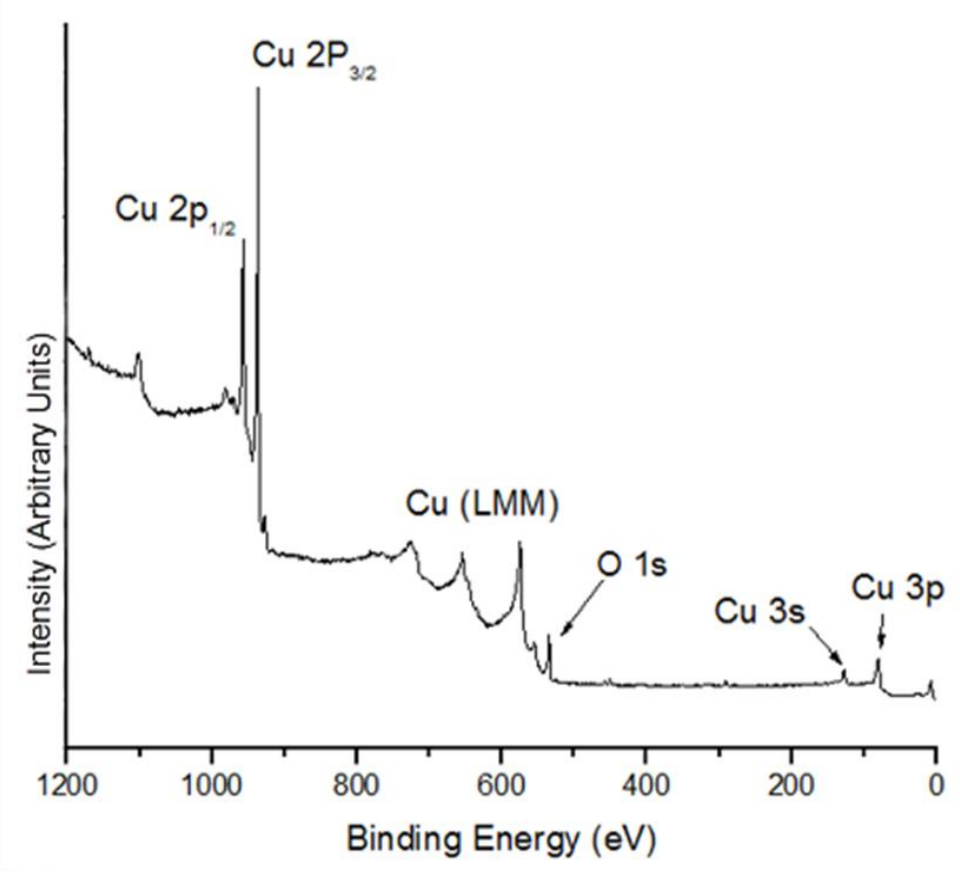

Figure 2.8 XPS broad scan of as purchased CuO powder sample.

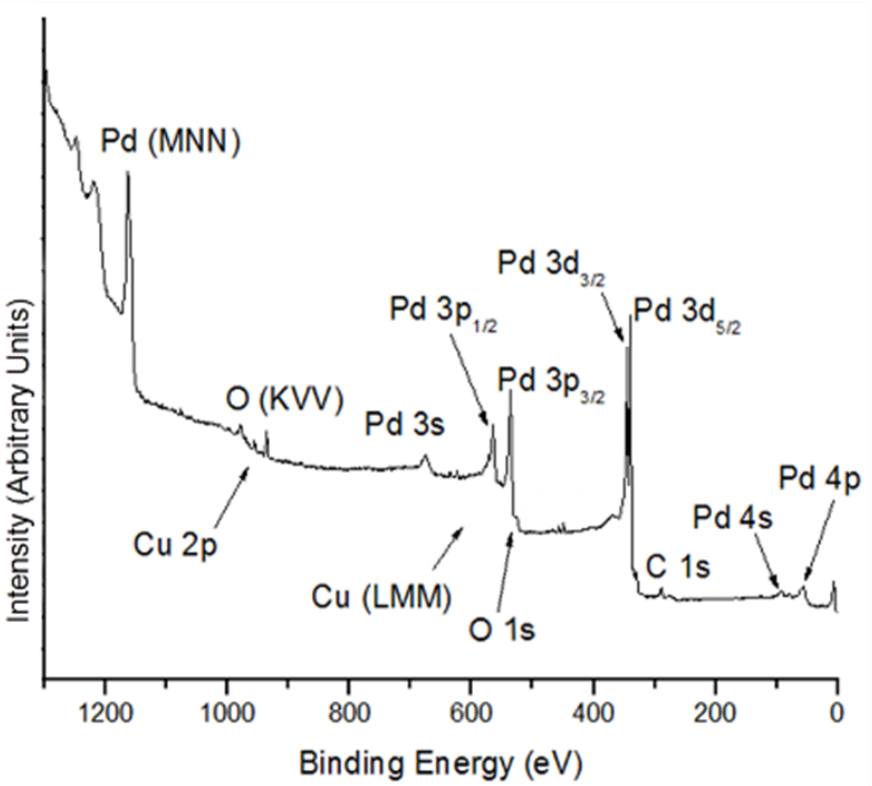

Figure 2.9 XPS broad scan of $Cu_{.05}Pd_{.95}O$ powder.

II. E. Auger Electron Spectroscopy

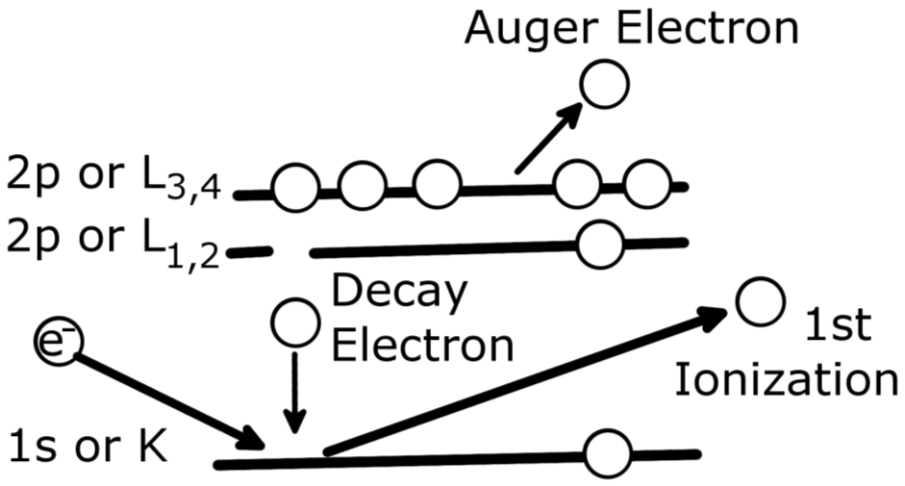

Figure 2.10: Auger process diagram.

AES spectra result from electrons produced through the three-electron Auger process, depicted in figure 2.10. The kinetic energy (KE) can be calculated as KE = E1 – E2 - E3, where KE is kinetic energy of the Auger electron, E1 is the energy of the first ionized electron, E2 is the energy of the "decay" electron and E3 is the energy of the electron ejected in the Auger process.

To generate an Auger spectrum, a sample is placed in ultra-high vacuum and is bombarded with electrons of a known energy. The kinetic energy of the Auger electron is then measured with the same electrostatic analyzer used in the XPS experiment. A spectrum can then be obtained by plotting the electron intensity vs. the kinetic energy passed by the analyzer. Figure 2.11 contains an Auger spectrum for a $Cu_{0.50}Pd_{0.50}O$ sample with labeled peaks for atoms comprising the solid solution. A differentiated spectrum is used to help reduce the effect of a high background when peaks are small. The background arises from electrons that have lost energy due to random inelastic collisions while escaping the sample surface. The mean free path of an Auger electron is typically 5 nm or less with energies between 40 and 2500 eV. Only Auger electrons within a few monolayers of the surface will escape with losing energy.

Figure 2.12 illustrates an Auger spectrum for a pure PdO sample. This is a broad scan, taken over a kinetic energy range of 100 to 1100 eV, and reveals Auger transitions for Pd and O. The carbon Auger peaks should appear at about 256 eV, but cannot be distinguished from the background in figure 2.13, and would otherwise overlap with the Pd peaks in figures 2.11 and 2.12. Figure 2.13 shows an Auger spectrum for a pure CuO sample. This is the broad scan for CuO and has peaks for Cu and O and allows for quick differentiation when compared to figure 2.12. The peak positions for both the pure

PdO and CuO samples may be compared to that of the solid solution sample in figure 2.11, which indicates that the contributions to the spectrum from the individual elements are well-resolved and can be used reliably for concentration measurements. Spectra were integrated in order to facilitate peak area determinations. Peak areas, often referred to as intensity, are compared and plugged into equation 1 in chapter 3. This equation uses sensitivity factors and peak areas to determine the atomic percent. Sensitivity factors can be determined experimentally using a known pure sample. A set of relative sensitivity factors normalized to a reference material can then be tabulated for each beam voltage.[65]

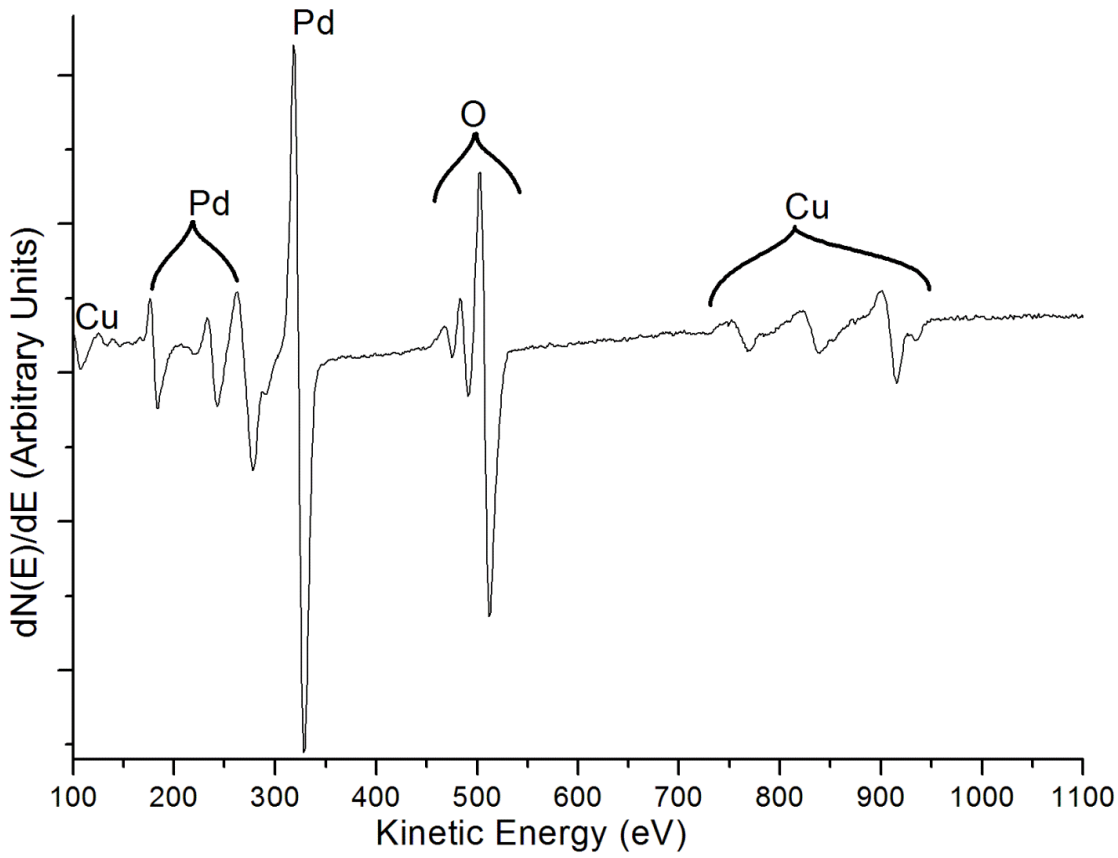

Figure 2.11 Differential Auger Spectrum of the $Cu_{0.50}Pd_{0.50}O$ solid solution.

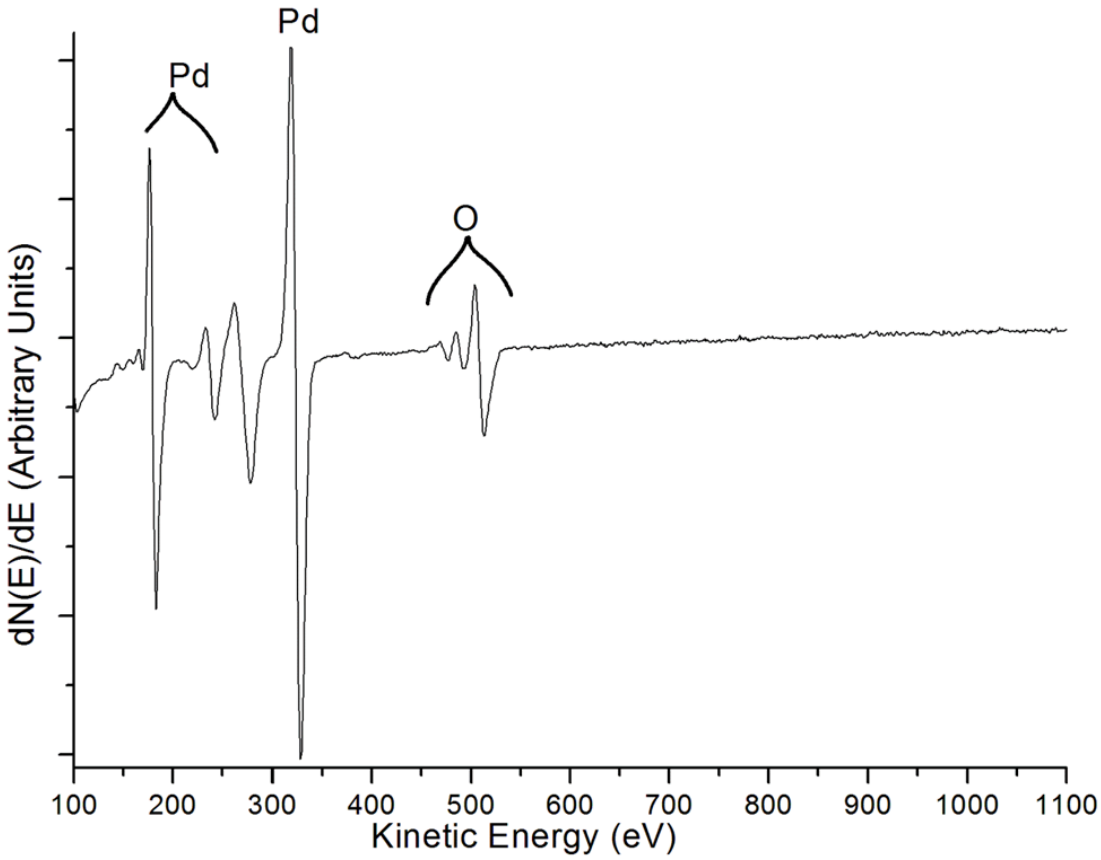

Figure 2.12 Differential Auger Spectrum of PdO.

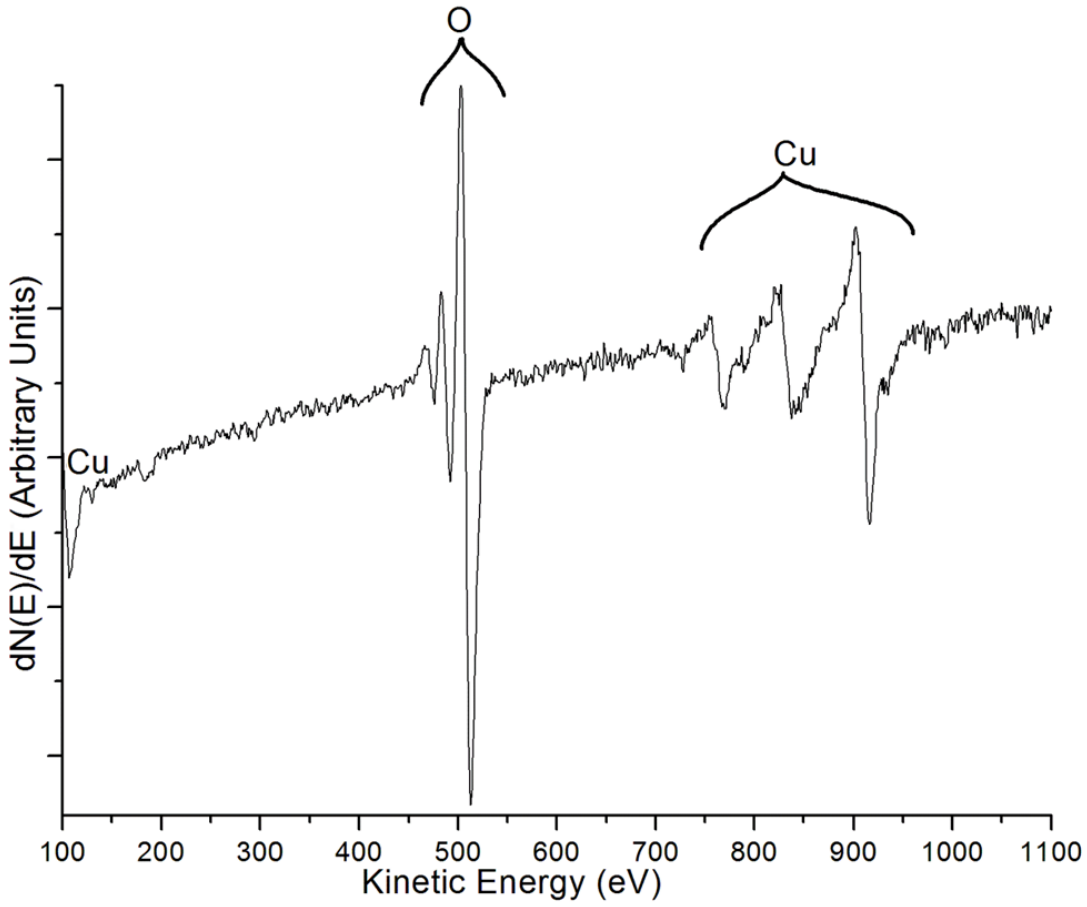

Figure 2.13 Differential Auger Spectrum of CuO.

These methods are well suited to the purpose of this study. X-ray diffraction is first used to identify the crystal structures present in each starting material CuO or PdO. These diffraction patterns are then used to reveal the solubility limit of CuO into the PdO lattice. XRD is able to clearly identify the two phases, even at low concentrations. XRD is also used to identify peak shifting due to the changes in the lattice parameters as a smaller Cu atom in substituted into the PdO lattice. Both XPS and AES characterizations are also performed. While XPS and AES are different techniques, they are done in the same vacuum chamber and both allow for the detection of atoms present

on the sample surfaces. XPS and AES give information that is used to calculate atomic concentrations of the sample surface. XPS uses X-rays to excite electrons in the sample while AES used electrons. This leads to very different spectra being obtained. XPS spectrums not only reveal what atoms are present, but they also reveal the chemical environment of each atom that is present. For example, the O peak from a metal oxide is different that an oxygen peak that arises from a hydroxyl group. This leads to the identification of the oxidation states present of many of the atoms. AES spectra are produced from the Auger process. These Auger electrons have energies that are specific to the atom and electron shell that the originate from. Further use of these characterization methods is discussed in the following chapters.

References

[47] Galdecka, E., International Tables for Crystallography **2006**, Vol. C, Ch. 5.3.1, pp. 505-508.

[48] Mahajan, R., Kumar, S., Prakash, R., Kumar, V., Synthesis and luminescent properties of Sn^{3+} activated lithium zinc borate phosphor, AIP Conference Proceedings **2006**, 030045 (2018); https://doi.org/10.1063/1.5051301.

[49] O'Connor, B. H., Raven, M. D., Application of the Rietveld Refinement Procedure in Assaying powdered Mixtures, Powder Diffraction, **1988**, 3(1), 2-6.

[50] Young, R.A., The Rietveld Method, edited by R.A. Young, IUCr Book Series, Oxford University Press **1993**, 1-39. "Introduction to the Rietveld method".

[51] Lee, D. W., Jin, M. H., Lee, Y. J., Park, J. H., Lee, C. B., Park, J. S., Reducing-agent-free instant synthesis of carbon-supported Pd Catalyst in a green Leidenfrost Droplet Reactor and Catalytic Activity in Formic Acid Dehydrogenation, Sci. Rep. **2016**, 6, 26474; doi: 10.1038/srep26474.

[52] Wu, Q., Rao, Z., Yuan, L., Jiang, L., Sun, G., Ruan, J., Zhou, Z., Sang, S., Carbon supported PdO with improved activity and stability for oxygen reduction reaction in alkaline solution, Electrochimica Acta 150, **2014**, 157-166.

[53] Cho, S. D., Park, H., Ionic liquid-assisted direct synthesis of PdO nanoparticles immobilized on boehmite nanoparticles, Journal of Colloid and Interface Science **2011**, 357, 46-49.

[54] Li, W. B., Murakami, Y., Orihara, M., Tanaka, S., kanaoka, K., Murai, K., Moriga, T., Kanezaki, E., Nakabayashi, I., XAFS and XRD studies of PdO-CeO_2 catalysts on x-Al_2O_3, Physica Scripta. **2005,** Vol. T115, 749-752.

[55] Wang, L., Lou, Z., Wang, R., Fei, T., Zhang, T., Ring-like PdO-NiO with lamellar structure for gas sensor application, J. Mater. Chem., **2012**, 22, 12453.

[56] Baylet, A., Marécot, P., Duprez, D., Castellazzi, P., Groppi, G., Forzatti, P., In situ Raman and in situ XRD analysis of PdO reduction and Pd0 oxidation supported on γ-Al_2O_3 catalyst under different atmospheres, Phys. Chem. Chem. Phys., **2011**, 13, 4607-4613.

[57] Ethiraj, A. S., Kang, D. J., Synthesis and characterization of CuO nanowires by a simple wet chemical method, Nanoscale Research Letters **2012**, 7:70.

[58] Volanti, D. P., Keyson, D., Cavalcante, L.S., Simões, A. Z., Joya, M. R., Longo, E., Varela, J. A., Pizani, P. S., Souza, A. G., Synthesis and characterization of CuO flower-nanostructure processing by a domestic hydrothermal microwave, Journal of Alloys and Compounds 459, **2008**, 537-542.

[59] Suresh, S., Karthikeyan, S., Jayamoorthy, K., FTIR and mulitvariate analysis to study the effect of bulk and nano copper oxide on peanut plan leaves, Journal of Science: Advanced Materials and Devices **2016**, xxx, 1-8.

[60] Volanti, D. P., Orlandi, M. O., Andrés, J., Longo, E., Efficient microwave-assisted hydrothermal synthesis of CuO sea urchin-like architectures via a mesoscale self-assembly, CrystEngComm, **2010**, 12, 1696-1699.

[61] XPS Peak4.1 on UK Surface Analysis: Forum Software Tools for Surface Analysis.http://www.uksaf.org/software.html (accessed Feb 19, 2013).

[62] Shirley, D. A., High-Resolution X-ray Photoelectron Spectrum of the Valence Bands of Gold. Phys. Rev. B **1972**, 5 (12), 4709−4714.

[63] Vegh, J., The Shirley Background Revisited. J. Electron Spectrosc. Relat. Phenom. **2006**, 151 (3), 159−164.

[64] Shchukarev, A. V., Korolkov, D. V., XPS Study of Group Carbonates, CEJC, 2(2), **2004**, 347-362.

[65] Narumand, D. H., Childs, K. D., Auger Spectrometers: A Tutorial Review, Applied Spectroscopy Reviews, **1999,** 34(3), 139–158.

Chapter 3 - $Cu_xPd_{1-x}O$ Solid Solution Characterization Study

III A. **Abstract**

$Cu_xPd_{1-x}O$ forms a homogeneous solid solution over the wide range[66] of $0 \leq x \leq 0.725$ in which compositional variation can be correlated with structural and chemical environmental changes. After a small lag at low Cu^{2+} concentrations, where the lattice cell parameters are pinned to that of the pure PdO structure, $Cu_xPd_{1-x}O$ lattice parameters follow Vegard's law in which the cell volume decreases linearly with x, indicating a homogenous solution in which Cu^{2+} randomly replaces the larger Pd^{2+} cation. The crystal structure also undergoes an increase in the c/a cell ratio, which relaxes the tetragonal distortion around the metal cation and shifts the metal-oxygen distance towards that of pure CuO (tenorite). X-ray photoelectron spectroscopy (XPS) shows a linear increase in Pd^{2+} 3d and Cu^{2+} 2p binding energies with increased Cu^{2+}, a result of the increased Madelung energy and relaxation effects which occur during the photoemission process. XPS and Auger Electron Spectroscopy (AES) indicate that the surface composition is comparable to that of the bulk, and copper XPS Auger parameter analysis confirms a different, and variable, environment for copper in $Cu_xPd_{1-x}O$ than is found in pure tenorite.

Key words: palladium oxide, copper oxide, XPS satellite structure, Vegard's law.

III B. **Introduction**

Transition metal oxides (TMOs) find use in a variety of catalytic and materials applications. In practice, working TMOs often comprise several transition metal compounds to tailor the material to the task at hand. For the monoxides PdO and CuO, the facile nature of oxygen exchange at their surface gives them extensive applications as gas sensors[67-79] and partial oxidation catalysts.[80-88] While both PdO and CuO exhibit catalytic activity towards oxidation of CO and various organic materials, PdO shows greater reactivity and thus is often used in total oxidation applications, as in methane turbines, whereas CuO shows milder, more selective partial oxidation behavior, as in methanol

synthesis. When combined, the effect can be cumulative, with palladium providing hydrogen spillover for CuO-initiated partial oxidation catalysis and perhaps helping reduce the CuO. However, there is evidence that the two oxides are symbiotic and that their admixture alters the basic physical properties of the sample beyond that expected by simply combining the two oxide materials. PdO and CuO form homogeneous solid solutions over a wide range of composition. The solid solution retains the PdO crystal structure, which places the copper in a distinctively different site than is found in CuO, but also varies the environment around the Pd^{2+} cation proportional to the copper content. We show that the surface properties of the solid solution also vary with copper content and differ from that of the two constituent single-metal monoxides.

PdO[89] and CuO[90] are both a p-type semiconductors. PdO adopts the $P4_2/mmc$ tetragonal lattice structure with lattice parameters of a = b = 3.0434 Å and c = 5.3363 Å, and a cell

volume of 48.93 Å^3.[91,92] The coordination in palladium oxide is approximately square planar around Pd^{2+}, with four equidistant oxygen ions, and O^{2-} in tetrahedral coordination. A distortion relaxes the palladium from a nominally D^9_{4h} space group, with equivalent Pd-O nearest-neighbor bond lengths of 2.024 Å but with pairs of O-Pd-O angles of $82.5^0/97.5^0$. CuO forms a monoclinic structure with lattice parameters of a = 4.6837(5) Å, b = 3.4226(5) Å, c = 5.12886(6) Å and $\beta = 99.54^o$, and a cell volume of 82.23 Å^3.[93] Found as the mineral tenorite, CuO nominally places Cu^{2+} in six-fold coordination; however the structure is severely distorted from an ideal octahedron. As in PdO, Cu^{2+} is also surrounded by four O^{2-} in approximate square planar coordination at ~ 2 Å, but has two more distant apical O^{2-} ions. The formal valence configuration of $4s3d^9$ makes the Cu^{2+} ion an ideal candidate for Jahn-Teller distortion, and the two apical Cu-O bond distances are elongated by about 42%, at 2.784Å, relative to the planar Cu-O nearest-neighbor bonds found at 1.95-1.96 Å. Thus, a solid solution of Cu dissolved into the PdO lattice should produce copper in a very different environment than that found in its native tenorite, one which can be viewed as the limiting case in Jahn-Teller distortion that completely removes the apical oxygen from the Cu^{2+} coordination sphere.

While both Pd^{2+} and Cu^{2+} form stable or metastable monoxide compounds under common ambient conditions; the ionic radius of Cu^{2+}, $r \approx 0.57$Å, is somewhat smaller than that of Pd^{2+}, where $r \approx 0.64$Å.[94] Yet, the two systems have been reported to form solid solutions over a wide range of miscibility.[95] Despite their technological significance, only a single study has reported on their bulk miscibility[95] and none has appeared that describes the surface properties or the chemical nature of the $Cu_xPd_{1-x}O$ solid solution.

In this study, solid solutions of CuO dissolved into PdO were synthesized with copper concentrations up to 72.5%, above which the material was found to phase separate into $Cu_{0.725}Pd_{0.275}O$ and CuO. The solid solutions were characterized with x-ray photoelectron spectroscopy (XPS), Auger electron spectroscopy (AES) and x-ray diffraction (XRD). Crystal structures and homogeneity were determined by XRD, which confirmed the solid solutions follow Vegard's law over a wide compositional range and demonstrated decreasing angular distortion from 90^o around the metal cation with increasing Cu^{2+} concentration. Surface composition was determined with both XPS and AES, and was found to be comparable to the bulk value. XPS data were also used in Auger parameter analysis and in determination of binding energies for the constituent elements, showing environmental changes for Pd^{2+} and Cu^{2+}, which varied with copper concentration as described below.

III C. Experimental Methods

Cupric oxide, black lot 754948, was obtained from Fisher Scientific Company Chemical Manufacturing Division. Palladium (II) oxide, lot 02704KJ, was obtained from the Sigma-Aldrich Company. Synthesis of solid solutions consists of grinding a sample of PdO and CuO in the desired stoichiometry with an agate mortar and pestle for ten minutes and compressing the powders with a stainless steel die and LooMis Engineering & MFG Company hydraulic pellet press at 15,000 psi for ten minutes to make a pellet of 23 mm diameter and approximately 1 mm thickness. The pellet was then placed in a furnace in air at 750 ^{0}C for at least three days and homogeneity was determined by powder x ray diffraction (XRD). To obtain solid solutions of 70 % or higher copper

concentration, it was necessary to perform the grinding and heating routine three times to obtain a single-phase, homogeneous material. Samples of lower concentration did not require these extra repetitive steps. The temperature of 750 ^{0}C was chosen to remain below the melting point of PdO,[96] but yet provide facile enough diffusion to form homogeneous samples within a reasonable timeframe.

All samples were characterized by XRD using a Bruker-AXS D8 Discover diffractometer equipped with a GADDS Area Detector to confirm the phases present and to determine lattice parameters. Scans were taken in transmission mode over a 2θ range of 0-100^0 with a step size of 0.03 ^{0}. A mirror exit slit size of 1.2 mm was used with pinhole slit size of 0.5 mm and a 0.5 mm snout. XRD analysis was performed using Topas 2.1 software.

AES and XPS analysis was performed using a Physical Electronics (Φ) model 15-255G double pass cylindrical mirror analyzer in pulse count detection for XPS and in lock-in mode for AES with the analyzer driven by a Perkin Elmer Φ 11-055 ESCA/Auger System Control. XPS photoemission was initiated with Al Kα radiation produced by a Φ 04-548 dual Mg/Al anode at 300 Watts and 15 KV using a Φ 14-040 X-ray generator. The XPS data were collected in 0.1 eV increments with a dwell time of 250 ms, and the spectra were signal averaged for 50-200 scans depending upon the element and concentration. Pass energies of 50 eV were employed, unless otherwise noted. AES spectra were initiated with a 2 KeV beam of electrons from a gun located concentric with the analyzer and controlled with a Φ Model 11-010 electron gun controller to produce a beam of 0.2 μamp/mm^2. Data were obtained in the dN(E)/dE mode and were summed for 5 scans, each taken in 1 eV increments with a time constant of 0.1 s and a lock-in modulation energy of 5 eV. XPS data were curve-resolved using XPSPeak 4.1

software.[97] A Shirley background[98,99] was used as a baseline for all peaks and the data were curve-resolved using a 20% Lorentzian/80% Gaussian sum. Examples of the curve-fitting procedure are given below.

Powder samples were freshly ground to produce a new surface prior to their admission into the ultrahigh vacuum chamber by use of a rapid transfer admissions system. The samples were mounted on clean indium foil for analysis and were measured by XPS and AES with no surface pretreatment or additional *in situ* UHV conditioning.

III D. Results

Evidence for bulk homogeneity of the $Cu_xPd_{1-x}O$ solid solutions is provided by powder x-ray diffraction. The XRD data in Figure 3.1 show the anticipated PdO diffraction pattern,[91,92] with features that shift to higher 2θ values as the copper concentration is increased, indicating a decrease in lattice parameters with increasing x. The XRD pattern of the tetragonal $Cu_xPd_{1-x}O$ unit cell is distinct from that of CuO (tenorite), and the data clearly indicate phase separation into $Cu_xPd_{1-x}O$ and CuO for traces in Figure 3.1 with $x \geq 0.75$, best seen in the intense (111) tenorite diffraction feature at 39^o.

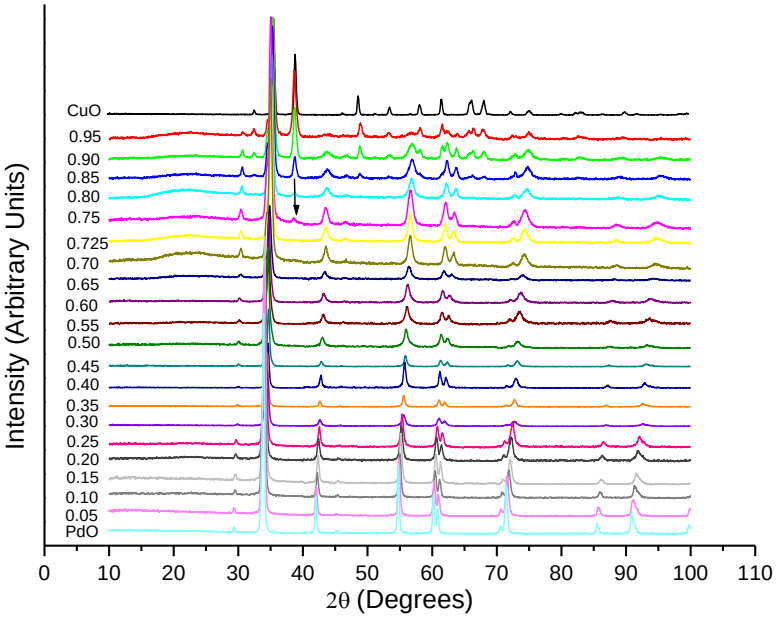

Figure 3.1 XRD of CuO/PdO as a function of copper concentration. Phase separation is detectable at $Cu_{0.75}Pd_{0.25}O$ and above, with diffraction features from CuO (tenorite) superimposed upon that of the solid solution at higher CuO ratios. The arrow indicates the most intense CuO peak position in the $Cu_{0.75}Pd_{0.25}O$ trace and the fractional copper concentration (x value) is indicated at the left side of each trace.

Lattice parameters were calculated using the Topaz 2.1 program, and the cell volume is plotted in Figure 3.2 as a function of copper concentration. The linear nature of the plot is an illustration of Vegard's law[100] in which the cell parameters vary smoothly with concentration over the range of single-phase formation in the solid solution. Extrapolation of the linear variation range to x = 1 predicts the unit cell parameters for pure CuO if it were to adopt the $P4_2/mmc$ PdO crystal structure. Adherence to Vegard's law is generally accepted as a measure of homogeneity in a solid solution where, in this case, Cu^{2+} randomly substitutes for Pd^{2+} in the PdO lattice. The data are somewhat noisier after phase separation due, in part, to the difficulty in fitting scattering from the $Cu_xPd_{1-x}O$ crystal structure in the presence of overlapping CuO diffraction features, but the scatter is also exacerbated by a greater difficulty in forming a

uniform, single-phase material close to the phase separation point. There is an apparent lag in the change in cell volume at the lowest copper concentrations ($x \lesssim 0.1$), indicating that low dopant levels of copper do not appear to affect the crystal lattice structure measurably. This lag in physical properties for low x values in $Cu_xPd_{1-x}O$ is also seen in other data presented below.

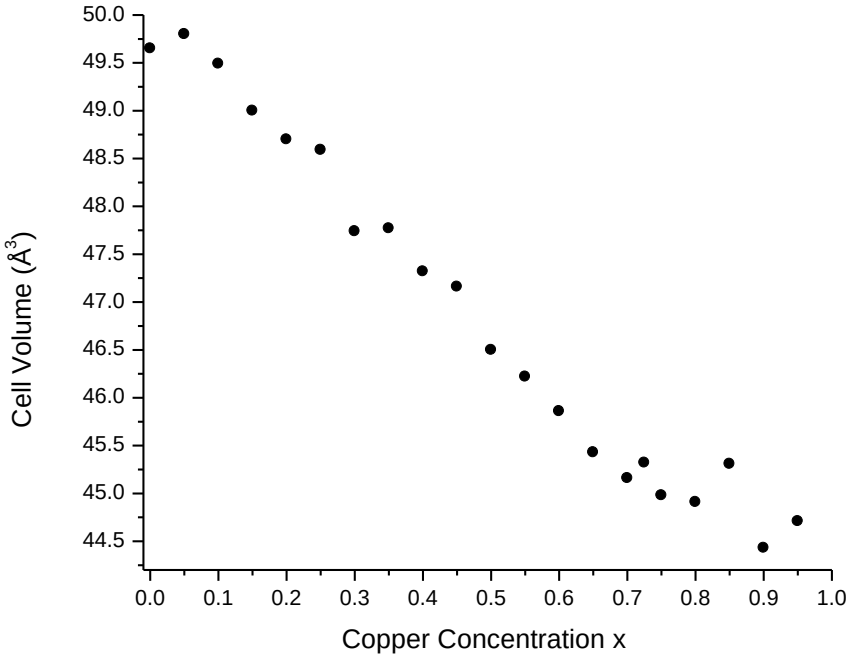

Figure 3.2 Lattice volume of $Cu_xPd_{1-x}O$ as a function of fractional copper concentration (x). The volume decreases linearly with x up to the point of phase separation ($x \approx 0.75$) after which the volume remains pinned to the phase-separated value, with some scatter in the data.

Individual lattice parameter variations and relative c/a unit cell parameter ratios are shown in Figure 3.3 as a function of copper concentration. It is interesting to note that while both lattice parameters decrease up to the point of phase separation, their ratio increases with increasing copper content. Thus, while the overall symmetry of the crystal structure is preserved in the solid solution, substitution of the smaller copper cation for

palladium causes an increased relative tetragonal elongation. This is illustrated pictorially in Figure 3.4 where, although the unit cell volume and unit cell parameters all decrease with dissolution of copper, the c unit cell parameter decreases at a more rapid rate than a to give a net increased c/a ratio. The increase in c/a partially removes the angular distortion of oxygen ligands found in PdO from the ideal 90^0 square planar geometry, with α increasing from 82.5^o to 83.1^o and β decreasing from 97.5^o to 96.9^o in PdO to $Cu_{0.725}Pd_{0.275}O$, respectively. While the lattice retains the PdO $P4_2/mmc$ tetragonal symmetry, the nearest neighbor M^{2+}-O^{2-} distance decreases from 2.02 Å in PdO to 1.96 Å in $Cu_{0.725}Pd_{0.275}O$, comparable to that of CuO (tenorite). There is an apparent lag in the onset of the increased tetragonal distortion, up to a solute concentration of approximately $x = 0.1$, as measured by the c/a unit cell parameter ratio, in the range where copper is initially added to the system. A deviation from Vegard's law is also seen in the individual lattice parameters at these very low copper concentrations; however, the trend is masked by a slight overall lattice expansion relative to pure PdO as copper is doped into the system at the lower concentration limits.

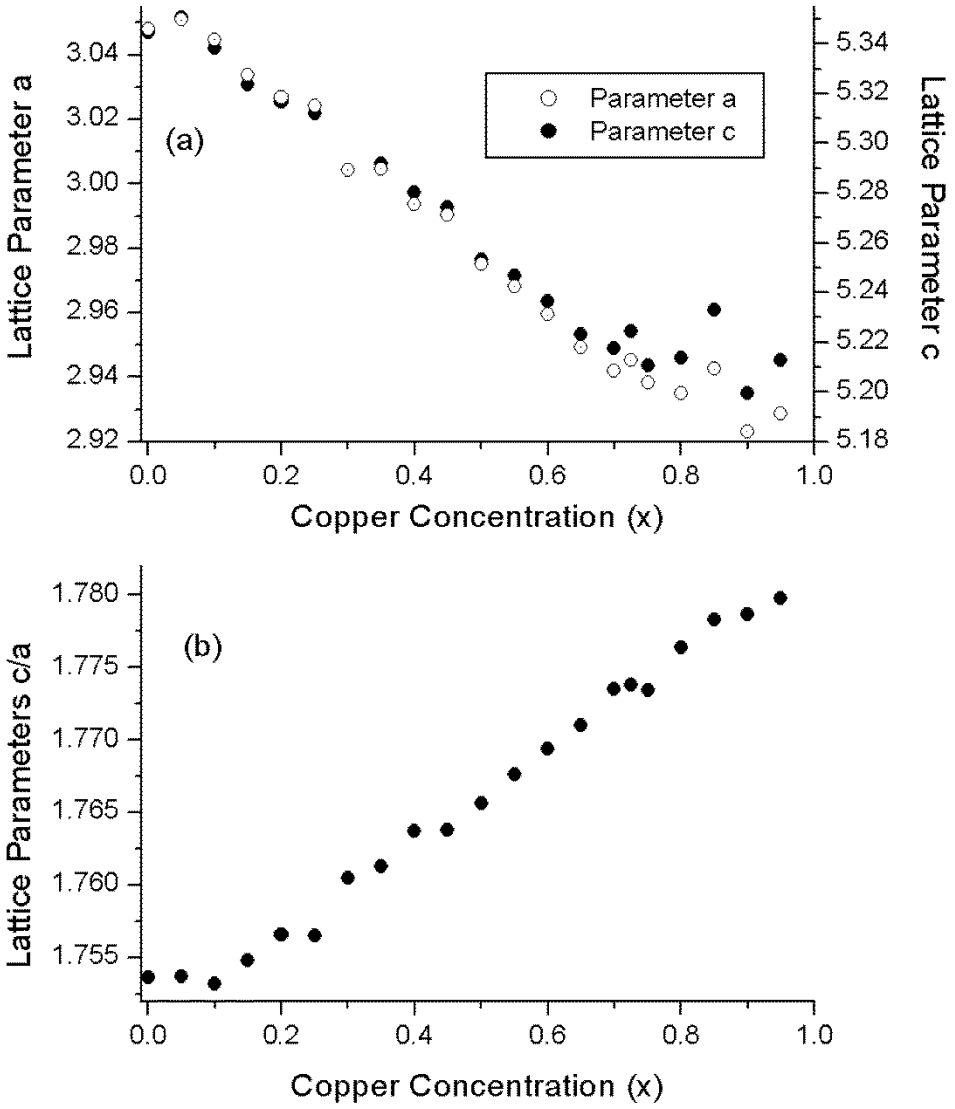

Figure 3.3 Lattice values for $Cu_xPd_{1-x}O$ as a function of fractional copper concentration (x value), a) lattice parameters a and c in angstroms and b) c/a parameter ratio.

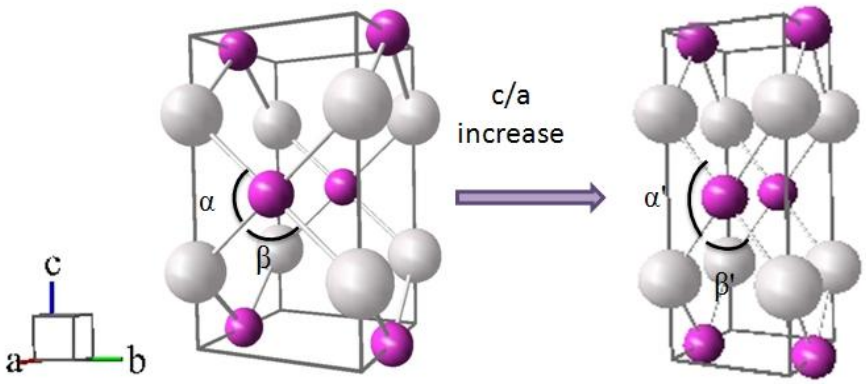

Figure 3.4 Schematic of effect of c\a increase on angular distortion around square planar Pd^{2+} coordination, where $\alpha = 82.5^{o}$ increases to $\alpha' = 83.1^{o}$ and $\beta = 97.5^{o}$ decreases to $\beta' = 96.9^{o}$ as x varies from 0 to 0.725 in $Cu_xPd_{1-x}O$. The distortion has been exaggerated for ease of illustration.

Auger electron spectroscopy (AES) was used to determine the copper and palladium surface concentrations in the solid solutions, which were then compared to that of the bulk. To accomplish this, the AES dN(E)/dE differential spectra that were obtained directly in lock-in detection mode were integrated to obtain N(E) data, and the areas under the N(E) peaks were obtained as a measure of integrated Auger intensity. For this study, AES peaks of interest included the Cu $L_3M_{4,5}M_{4,5}$ transition at approximately 920 eV and the Pd $M_5N_{4,5}N_{4,5}$ transition at approximately 330 eV. Eqn. 1 was used to determine $x_{surface}$, the fractional copper metal content at the surface:

$$x_{surface} = \frac{I_{Cu}/S_{Cu}}{I_{Cu}/S_{Cu}+I_{Pd}/S_{Cu}} \qquad (1)$$

where I_i is the integrated Auger intensity of peak i (i = Cu or Pd) and S_i is the sensitivity factor for i specific to the transition and analyzer.[101] Eqn. 1 assumes a homogeneous distribution of metals within the Auger sampling depth of approximately 50-100 Å. The data are presented in Figure 3.5, and indicate that the surface concentration is equal to

that of the bulk to within the error of the measurement with perhaps a slight deviation at x $\lesssim$ 0.1.

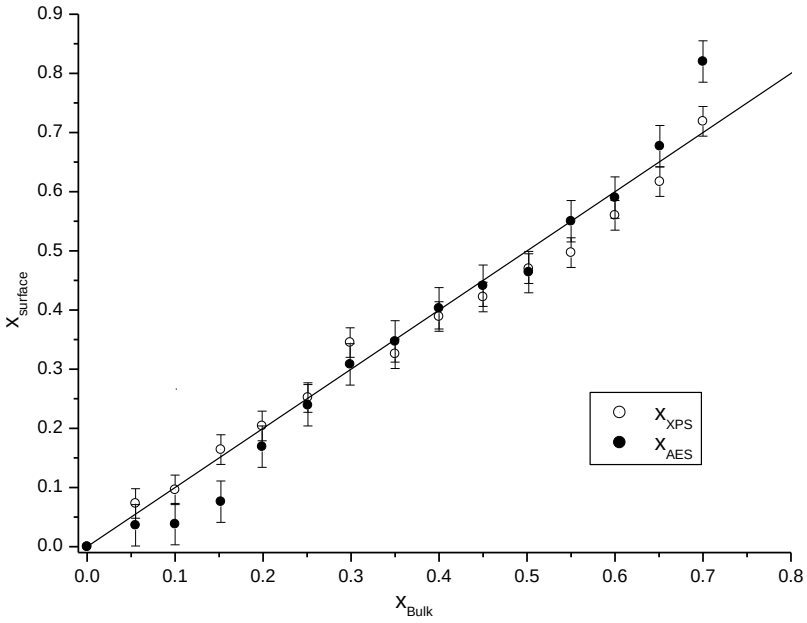

Figure 3.5 Surface vs. bulk copper concentration determined by XPS and AES. Error bars are estimated from the uncertainty in the peak fitting routine.

Eqn. 1 can be adapted for XPS analysis by use of core-level integrated photoemission data along with the appropriate sensitivity factors for the specific transitions employed.[102] XPS analysis of Cu $2p_{3/2}$ and Pd $3d_{5/2}$ intensities corroborates the results obtained with the AES measurements. Surface compositions correlate directly with bulk values, and the linear function that is found when $x_{surface}$ is plotted as a function of x_{bulk} yields a slope of 1.118 ± 0.006 for AES and 0.940 ± 0.005 for XPS, where errors are given as the statistical value resulting from linear regression. While both AES and XPS are surface-sensitive techniques, AES is slightly more surface-sensitive to palladium due to the lower kinetic energy of Pd $M_5N_{4,5}N_{4,5}$ relative to Cu $L_3M_{4,5}M_{4,5}$ used in the Auger measurements, but XPS is slightly more surface-sensitive to copper due to the

lower kinetic energy of the Cu 2p core photoelectron relative to that of Pd 3d transition used in the XPS analysis. That the two techniques with slightly different surface penetration depths give similar surface concentrations supports the assumption of uniform concentration in the near-surface region.

XPS peak shapes and binding energies provide greater detail of the chemical environment for palladium and copper in the solid solutions. Figure 3.6a shows XPS data for the Pd 3d region as a function of copper content. The pure PdO spectrum presents characteristic $3d_{5/2}$ and $3d_{3/2}$ main peaks at 336.43 eV and 341.70 eV, respectively, and shows very weak satellite structure with intensities of $\approx 15\%$ relative to the main peak in agreement with literature data.[113,103-109] As copper is added to the PdO lattice, the overall palladium 3d XPS intensity decreases as a result of palladium dilution by copper. However, the peak shape remains comparable to that of pure PdO throughout the series. Satellite structure in transition metal oxides is often intense and very characteristic of the TMO valence band character due to highly-correlated electrons in the partially-filled d orbitals, and NiO with a $3d^8$ valence configuration is a prototype for this effect.[110-112] Pd is directly below Ni in the periodic table and while PdO also shows electron correlation[113,114] the diffuse nature of the $4d^8$ Pd^{2+}orbitals makes the interaction weak which results in less intense satellite structure for the palladium oxide. Because of the weak intensity of the satellite and the problem of accurately resolving it from the background and the main peaks, the positions and intensities of the weak satellite structure are difficult to fit precisely. Figure 3.6b illustrates the peak fit procedure used to analyze the $Cu_xPd_{1-x}O$ materials for pure PdO and for the $Cu_{0.65}Pd_{0.35}O$ solid solution.

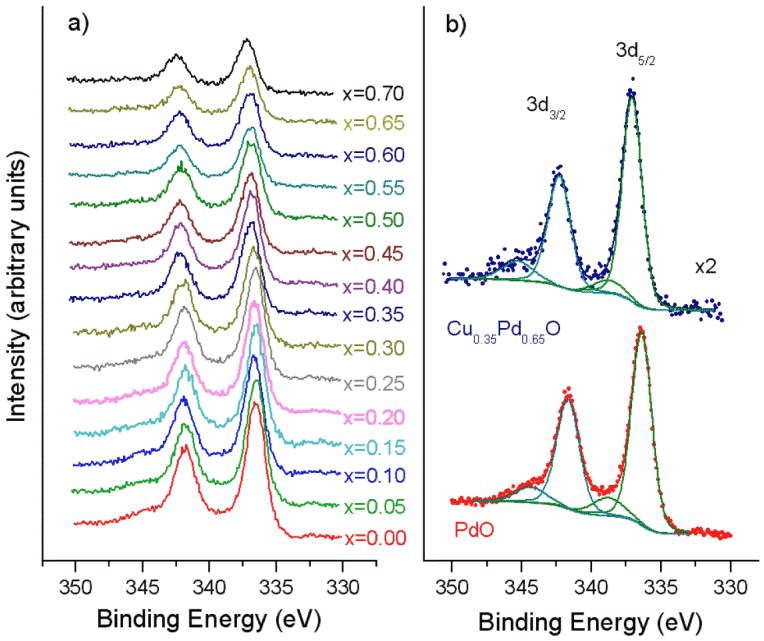

Figure 3. 6 Pd 3d XPS for $Cu_xPd_{1-x}O$ solid solution spectra a) as a function of copper concentration (x value), and b) with representative peak fits. The experimental data are represented as circles, with the fits given as solid lines. Details of the peak fitting are documented in the experimental section.

While the peak shape and satellite structure remain constant to within the error of the XPS measurement and curve resolution, the main peak binding energies show a definite shift to higher binding energy with increasing copper concentration. The Pd $3d_{5/2}$ and $3d_{3/2}$ main peak binding energies are plotted as a function of copper concentrations for $Cu_xPd_{1-x}O$ solid solutions in Figure 3.7, which indicates a clear shift to higher binding energy with increased copper content. The data are calibrated relative to two different "standard" peaks in the $Cu_xPd_{1-x}O$ XPS spectrum, adventitious carbon, taken to have C 1s = 284.60 eV and lattice oxygen with O 1s = 529.83 eV. Adventitious carbon, resulting from exposure to ambient contamination, is extensively used as calibrant for XPS.[115] However, it is not always present in sufficient amounts to give good C 1s spectral intensity and it is not strictly an internal calibrant, being heterogeneously mixed with the

sample and sometimes developing contact potential differences that lead to errors in the binding energy values. The lattice O 1s binding energy often remains constant upon adsorption or dissolution of guest materials in TMO oxides,[110] and is a true internal calibrant. As can be seen in Figure 3.7, the two different calibrants yield comparable values, although reference to C1s yields slightly noisier data. Binding energies for the Pd 3d transitions are summarized in Table 3.1.

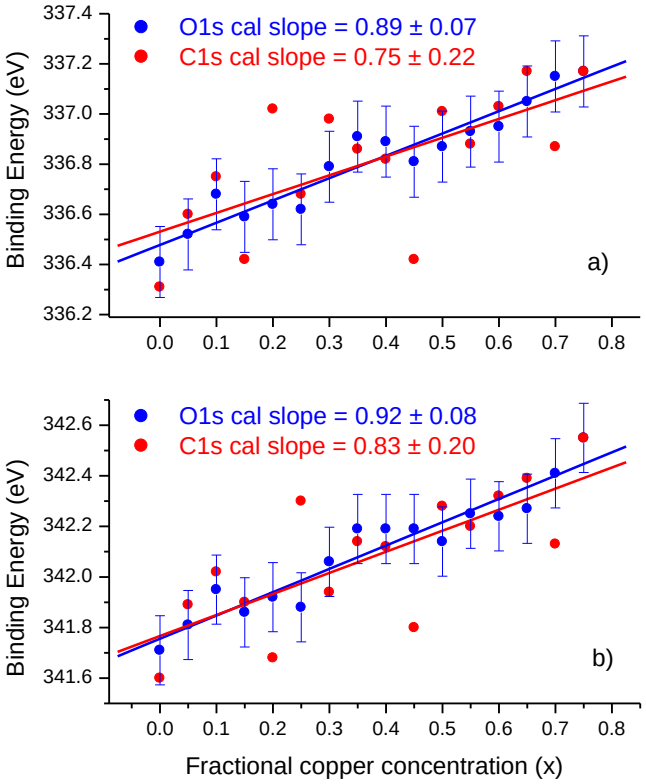

Figure 3.7 Pd 3d binding energies for $Cu_xPd_{1-x}O$ solid solutions, calibrated relative to O 1s at 529.8 eV and C 1s at 284.6 eV for the a) $3d_{5/2}$ and b) $3d_{3/2}$ transitions. Error bars reflect uncertainty in measuring peak positions whereas error in slope results from linear least squares analysis.

Figure 3.8 shows Cu^{2+} 2p XPS data for monoclinic CuO (tenorite) along with that for the tetragonal $Cu_xPd_{1-x}O$ solid solutions. The Cu 2p peak structure is complex, with

intense satellite peaks that remain fairly consistent in peak shape and intensity across the series. The structure is characteristic of the late 3d transition metal oxides with a partially-filled valence band that hybridizes with the O 2p band, [116] as described by the charge-transfer insulator model.[112,117]

$$\Psi_{vb} = 3d^n + \alpha\, 3d^{n+1}\,\underline{L} \qquad (2)$$

In eqn. 2, Ψ_{vb} is the ground state valence band structure of the oxide, $\underline{L}$ represents a hole in the O 2p valence band and α is a mixing parameter that determines the amount of 3d – O 2p hybridization. Upon photoemission of a copper 2p core electron, overlap between Cu 3d and O 2p leads to final state effects where the screened $2p^5 3d^{n+1}\underline{L}$ state is approximately 9 eV lower in binding energy than the unscreened $2p^5 3d^n$ state, as is labeled in Figure 3.9b.[117,118-122] The "main" peak, comprising peaks A and B in Figure 3.8c, represent the screened $2p^5 3d^{n+1}\underline{L}$ final state with the individual features due to local and nonlocal screening, the former term describing a final state that primarily involves a hole created on the nearest-neighbor oxygen atoms surrounding the copper ion undergoing photoemission and the latter involving a more delocalized hole in the O 2p band structure. Delocalization of the O 2p hole helps ameliorate repulsive O 2p hole - Cu 2p hole interactions and cluster calculations carried out on copper oxide models[119] assign the lower binding energy A peak to the non-locally screened $2p^5 3d^{n+1}\underline{L}$ final state and the higher binding energy B peak to the locally-screened state. The combined "satellite" peaks C and D represent the unscreened $2p^5 3d^n$ final state, the peak structure of which reflects the spin-orbit multiplet structure of the partially-filled 3d valence band.[119] Due to the partially-filled nature of the strongly electron-correlated 3d band, the spectrum reflects a complex set of closely-lying final states resulting from multiplet splitting[123] and

other effects.[124,125] However complicated the constituent states contributing to the photoemission, the shape for each feature is generally curve-resolved into a set of two Gaussian-Lorentizian peaks as shown in Figure 3.8b. The background is particularly difficult to approximate for the Cu 2p spectrum due to the wide energy range and the large, cumulative secondary electron contribution at the high binding energy of the Cu 2p transition. Quantitative analysis has therefore been restricted to the $2p_{3/2}$ contribution, as shown in Figure 3.8c.

The peak shapes and relative intensities of the copper photoemission have been related to the stoichiometry and the band structure of the copper oxides. The relative intensity of the unscreened (C+D) to screened states (A+B) for pure tenorite (CuO), measured here to be $(I_C+I_D)/(I_A+I_B) = 0.47$, is in good agreement with literature values.[121,126] However, the solid solutions appear to provide the copper ion with less efficient access to the screened final state, and the unscreened/screened $(I_C+I_D)/(I_A+I_B)$ ratio for $Cu_{0.05}Pd_{0.95}O$ is significantly higher at $(I_C+I_D)/(I_A+I_B) = 0.66$. As shown in Figure 3.9, the ratio decreases with increase in copper concentration, approaching that of CuO at higher x values as the Cu-O bond length decreases from the longer metal-oxygen distance for low copper concentration $Cu_xPd_{1-x}O$ solid solutions to that more closely approximating that found in CuO. The individual component ratios, $I_A/I_B = 1.0 \pm 0.3$ and $I_C/I_D = 1.1 \pm 0.5$, remain constant to within error for the solid solutions and compare to the pure CuO value of $I_A/I_B = 0.92$ although the pure CuO $I_C/I_D = 1.8$ is slightly higher. Both pure CuO I_A/I_B and I_C/I_D ratios measured here compare well to literature values.[121] Thus the copper 2p spectrum is qualitatively similar to that found for literature

CuO data, although the relative rate of the screened photoemission channels is somewhat lower relative to that of the unscreened state.

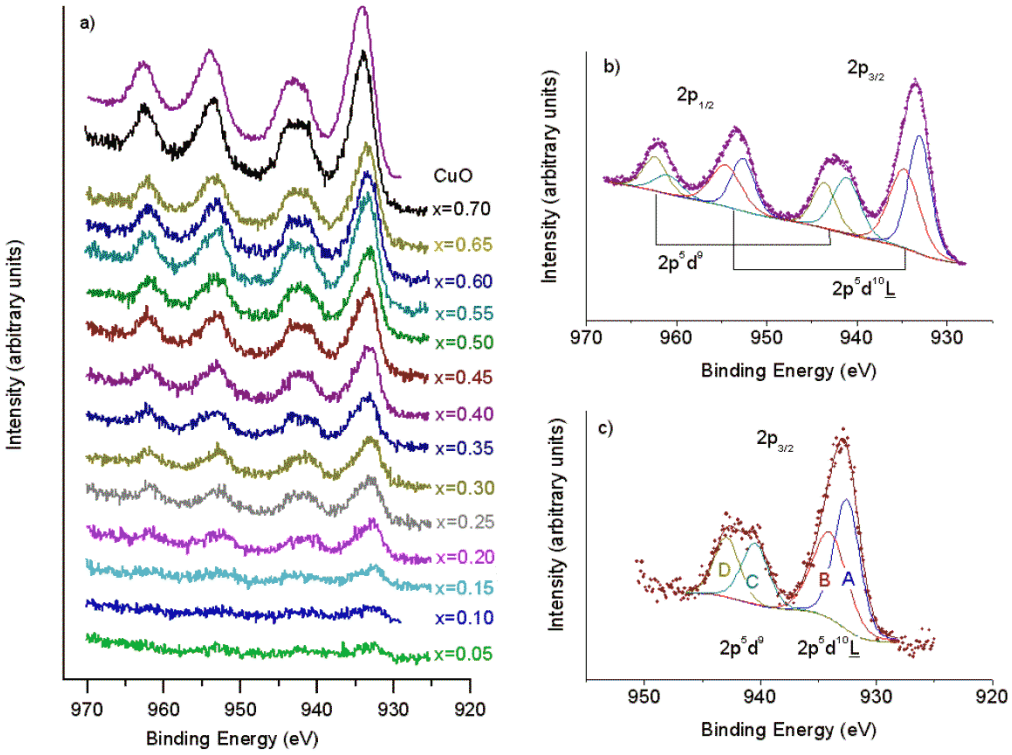

Figure 3.8 Cu^{2+} 2p XPS spectra a) as a function of copper concentration (x value) in $Cu_xPd_{1-x}O$ solid solutions, b) for CuO fit with a modified Shirley background (straight line + Shirley) over the entire 2p region and c) $2p_{3/2}$ region for $Cu_{0.45}Pd_{0.65}O$ spectrum with a simple Shirley background.

The nonlocal component of the main $2p^5 3d^{n+1}\underline{L}$ peak (A) and both unscreened $2p^5 3d^n$ satellite peaks (C and D) shift to higher binding energies with increase in copper concentration, as shown in Figure 3.10. From the viewpoint of the copper, this is perhaps unsurprising since the PdO lattice environment initially places the Cu-O bond length at longer distances than found in pure CuO (2.024 Å *v.s.* 1.95-1.96 Å) and these distances shorten significantly as the copper concentration increases in the $Cu_xPd_{1-x}O$ solid

solutions. However, the palladium core binding energy also shows a substantial binding energy shift of almost 1 eV to higher values (Figure 3.7). Since final state effects play an insignificant role in Pd core photoemission and since the main contribution to the satellite peaks in Cu is unscreened, binding energy shifts for these features can be described in terms of initial state effects and core hole relaxation effects.

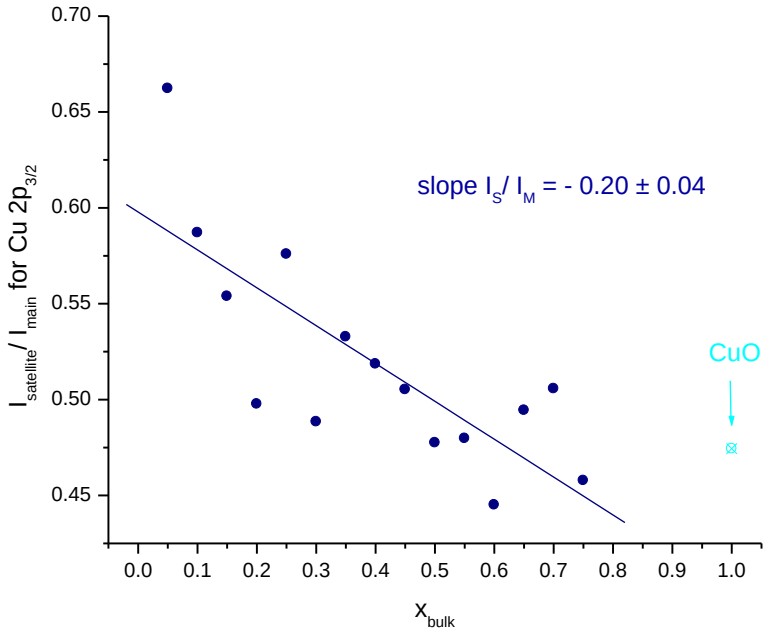

Figure 3.9 Satellite to main peak intensity ratio for the Cu $2p_{3/2}$ transition for the $Cu_xPd_{1-x}O$ solid solutions as a function of copper concentration (x).

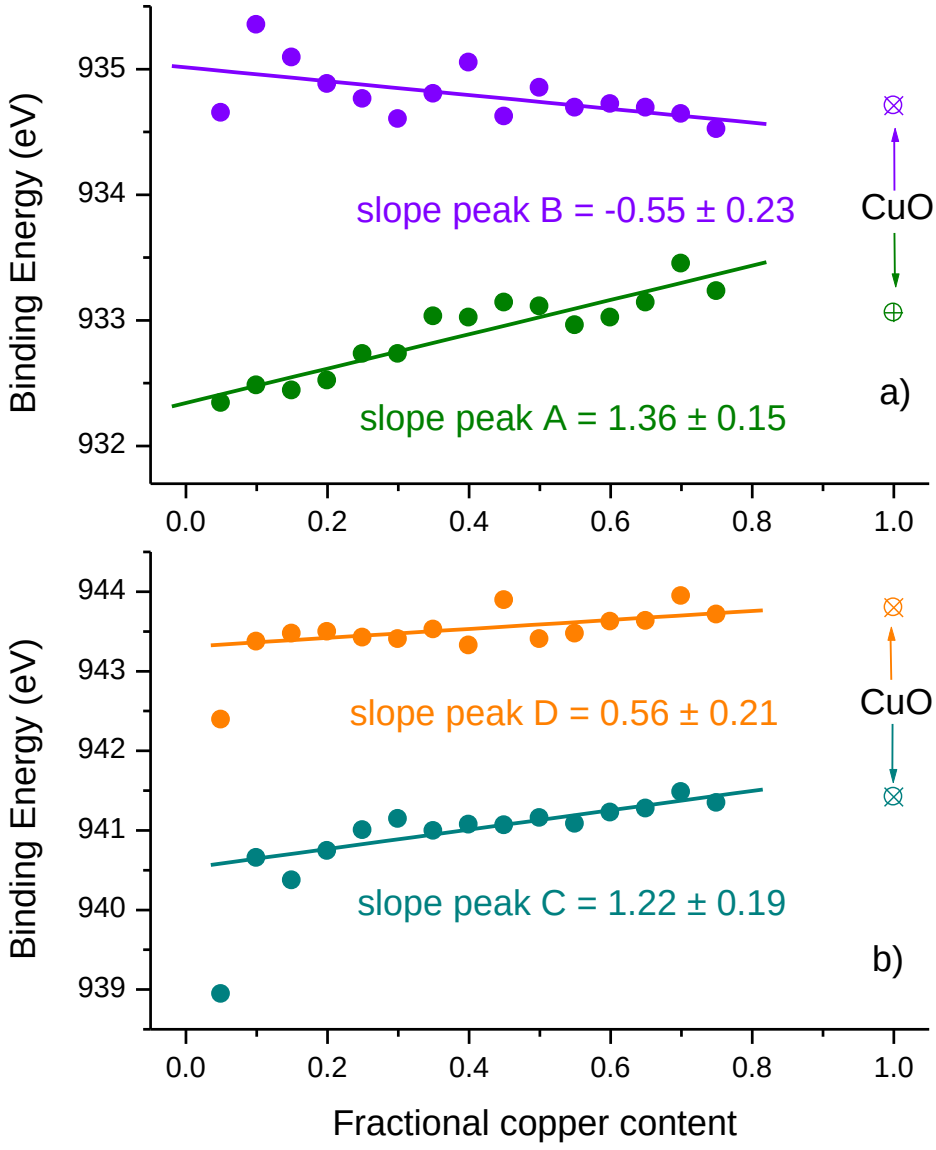

Figure 3.10 Cu 2p intensities for a) the main ($2p^5 3d^{10}\underline{L}$) peak component s and b) the satellite ($2p^5 3d^9$) peak components, with A, B, C and D obtained by fitting as illustrated in Figure 3.9c.

Binding energy shifts for compound oxides in the absence of final state effects have been successfully modeled for oxides through a simple formula[127,128]

$$\Delta E_b(A) = kq_A + Mad(A) + E_A^{rel} \qquad (3)$$

where $\Delta E_b(A)$ is the binding energy shift between the free atom A and the atom in the oxide, q_A is the valence charge on the atom in the oxide, k is a proportional coefficient that relates this charge to the potential energy due to the valence charge and can be approximated as the derivative of the core potential on atom A with respect to charge.[129] The kq_A term is responsible for the general rule of thumb that binding energies for a given element shift to higher values in XPS as the oxidation state of the element increases. The term E_A^{rel} corrects for relaxation effects and Mad(A) is the Madelung energy, defined as

$$Mad(A) = -\sum_{B \neq A} \frac{q_B}{r_{A-B}} \qquad (4)$$

Eqn. 4 sums over all other ions in the crystal except for the central cation A, q_B is the charge on the other cation in the sum and $r_{A\text{-}B}$ is the distance from A to the B coordination shell. The Madelung energy is positive for cations, where negatively charged terms from the anions outweigh the positive terms from the cations, and negative for anions. Equation (3) can be adapted to the present analysis by considering the changes that occur in the various parameters as a function of increased copper concentration.

The Madelung constant for the oxygen anion is negative in eqn. 3 and tends to balance the positive relaxation term for oxygen in oxide lattices, making the O 1s binding energy shift dependent on the valence charge term.[128] The O 1s binding energy remains constant to within the error of the measurement across the $Cu_xPd_{1-x}O$ series and it is, therefore, unlikely that the first term, kq_A, changes significantly for the lattice oxygen. Since it is difficult to imagine how the charge on the cation could vary without a corresponding change in the compensating anion, we assume that the first term varies

negligibly for the Cu^{2+} and Pd^{2+} cations in the solid solutions. In eqn. 3, both $Mad(A) + E_A^{rel}$ are positive for the cations, and the shift in binding energies observed within the solid solution series, shown in Figures 3.7 and 3.10, will reflect a positive shift in binding energy from the Madelung term since the lattice contraction that occurs with increased copper concentration will result in a decrease $r_{A\text{-}B}$, and therefore a larger positive Mad(A) contribution as x increases.

For the main components of the copper 2p photoemission peaks, final state effects modeled by valence band "shake up" transitions must be considered as well. All copper and palladium peaks show a positive shift in binding energy except for Cu peak B, implying that the final state core hole screening becomes less efficient as copper is added to the system. Cluster calculations[119] have assigned this peak to the locally-screened $2p^5 3d^{10}\underline{L}$ Cu 2p final state with non-local screening a lower binding energy due to lowering of hole-hole repulsion due to delocalization of the hole in the O 2p valence band. Cu core hole – O 2p valence band hole repulsion would be further exacerbated by a decrease in the Cu-O bond length, as occurs as copper is added to the system, and the shift to lower binding energy for peak B is attributed to final state effects.

Auger parameter analysis is also helpful in elucidating changes that occur upon formation of the $Cu_xPd_{1-x}O$ solid solution. The modified Auger parameter, α', is defined as: [130,131]

$$\alpha' = KE_{AES} + BE_{PES} \qquad (5)$$

where KE_{AES} is the kinetic energy of an Auger electron and BE_{PES} is the binding energy of a core-level photoelectron from the element of interest. The Auger parameter is useful

in distinguishing among different ligand environments for the photoemitting atom, including different coordination numbers, bond lengths and polarizability of the surrounding next-nearest neighbor ligand anions. Since both electron energies are obtained in the XPS spectrum on the same sample under identical spectral conditions, the Auger parameter has an added benefit that no corrections are need to compensate for surface charging.

Figure 3.11 shows the Auger parameter variation as a function of copper concentration for α' calculated using the Auger transition $CuL_3M_{45}M_{45}$ at a kinetic energy of approximately 918 eV and the core Cu $2p_{3/2}$ main photoemission peak maximum binding energy at approximately 933 eV (Table 3.2). As can be seen, the Auger parameter initially is found with values that lie well below that of CuO and, while the parameter values increase with copper concentration, they level out at a value that is still approximately 0.6 eV smaller than that found in CuO, in agreement with the tendency of the Auger parameter to increase with increased coordination.[131] As with the unit cell lattice parameter variation in Figures 3.2 and 3.3, there is a small lag in Auger parameter variation at low copper concentrations. The shift in the Auger parameter has been related to relaxation effects involving polarization from small electron density changes on the surrounding ligands[130,131]

$$\Delta\alpha' = 2\,E_A^{rel} \qquad (6)$$

in response to the creation of the photoelectron core hole. While eqn. 6 is strictly valid only for Auger parameters involving photoemission without final state effects, if we assume that final state effects that contribute to peak A in the Cu $2p_{3/2}$ main photoemission feature are constant within the series, the external relaxation effects are

found to increase with increased copper concentration in agreement with the shortening of the Cu-O nearest neighbor bond.

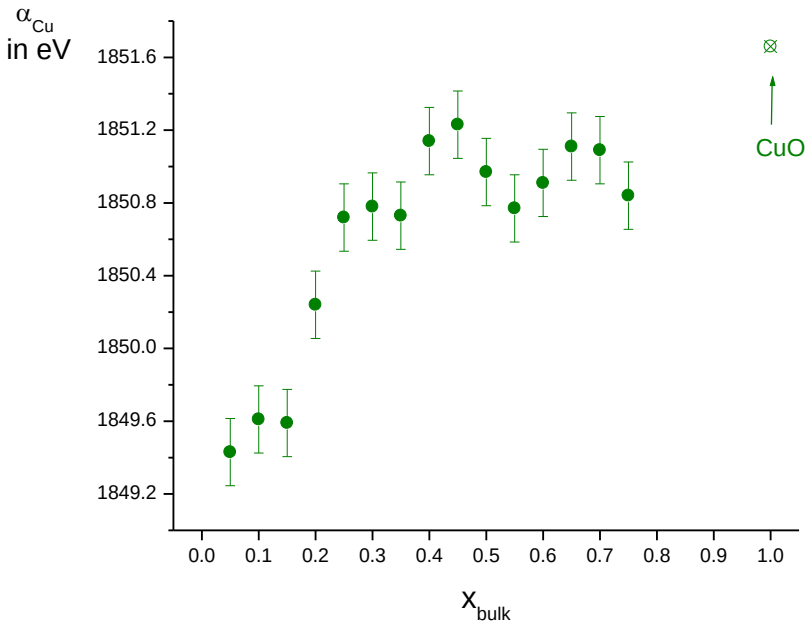

Figure 3.11 Copper Auger parameter as a function of copper concentration, x. Values of the solid solution approach a value of 1851 eV for high copper concentrations, still significantly less than that found in CuO tenorite.

Auger parameter analysis on the palladium component is, unfortunately, less successful due to the absence of a suitable Auger transition in PdO. In order for Auger parameter analysis to be performed with any precision, a sharp, distinctive Auger transition must be employed and upon oxidation all palladium Auger transitions accessible with the Al Kα x-ray anode used here become rounded with a poorly defined peak maximum. Attempts to locate a maximum in the Auger transition by differentiation and peak fitting did not yield consistent results for either the Pd Auger transitions, $M_{4,5}N_{2,3}V$ at $KE_{AES} \approx 273$ eV and M_5VV at $KE_{AES} \approx 327$ eV. While the two palladium

Auger parameters calculated using these transitions, $\alpha_1' = KE_{AES}(\mathrm{M_{4,5}N_{2,3}V}) + BE_{PES}(3d_{5/2})$ at 609.7 ± 0.3 and $\alpha_2' = KE_{AES}(\mathrm{M_{4,5}VV}) + BE_{PES}(3d_{5/2})$ at 663.8 ± 0.3, are within error of that obtained for pure PdO, no clear trend in variability can be found within the series. The palladium Auger parameter data are summarized in Table 3.1.

Finally, the O 1s region for the PdO, $Cu_xPd_{1-x}O$ and CuO samples is shown in Figure 3.12 The region is partially obscured by the Pd $3p_{3/2}$ photoemission feature,[109] which is most problematic for pure PdO and low x-content (high Pd concentration) samples. The lattice oxygen peak at 529.83 eV is easily resolvable for all samples with curve fitting, as described above. A weaker peak, found at approximately 531.5 eV, is only clearly apparent in spectra with low Pd $3p_{3/2}$ intensity. At approximately 15-25% the intensity of the oxide lattice peak, the intensity of the 531.5 eV peak is reasonable for monolayer –OH formation atop the surface of the oxide material upon brief exposure to the ambient air during the transfer into the UHV system. Under-coordination lattice sites or other species intrinsic to the polycrystalline oxide surface have also been suggested as a possible assignment for similar features in other metal oxide XPS investigations.[132] With the exception of the weak 531.5 eV feature, the O 1s spectrum is free of contamination and is well-resolvable. It serves as a good internal reference for the $Cu_xPd_{1-x}O$ solid solutions.

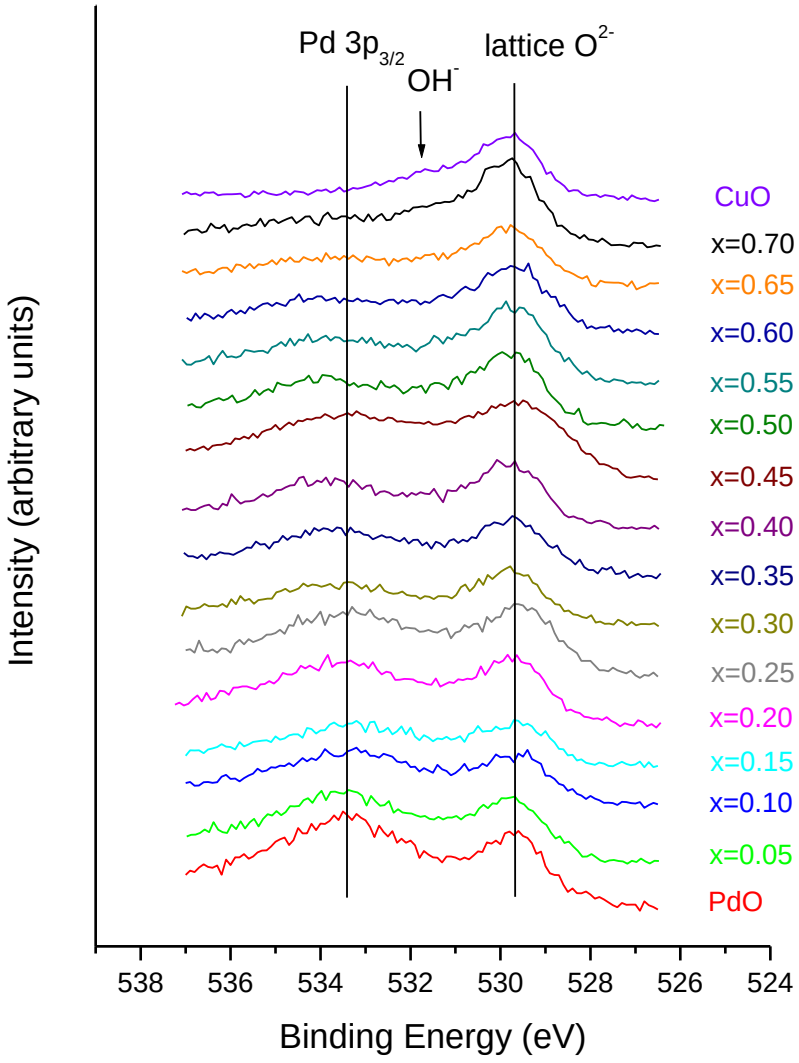

Figure 3.12 O1s XPS spectral region for $Cu_xPd_{1-x}O$ solid solutions as a function of copper concentration (x). The lattice oxygen and $Pd_{3/2}$ core photoemission peaks are indicated with vertical lines, as labeled in the figure, and the approximate position of the hydroxyl species is indicated by the arrow.

Table 3.1 Pd XPS data for core level binding energies, kinetic energies of Auger transitions and Auger parameters, all in eV. Kinetic and binding energies were calibrated relative to the lattice O 1s, taken to be at 529.83 eV.

	PdO	solid solution[a]	literature[b]
Pd^{2+} $3d_{5/2}$	336.43	336.51-337.23	336.0-336.8
Pd^{2+} $3d_{5/2}$ satellite	338.47	339.09-337.89	
Pd^{2+} $3d_{3/2}$	341.70	342.53-341.83	341.9-342.5
Pd^{2+} $3d_{3/2}$ satellite	344.29	345.66-344.16	
O 1s lattice	529.83	529.83	529.65
Pd $M_{4,5}N_{2,3}V$ (as kinetic energy)	273.0	273.0	273.6
α_1 (Auger parameter 1)	609.4	609.7	609.7
Pd M_5VV (as kinetic energy)	327.1	327.2	327.5-327.8
α_2 (Auger parameter 2)	663.5	663.8	662.9

[a]Solid solution Pd 3d binding energies vary with x, as shown in Figure 3.7.
[b]Literature references taken from refs. 113,103-109.

Table 3.2 Cu XPS data for core level binding energies, kinetic energies of Auger transitions and Auger parameters, all in eV. Kinetic and binding energies were calibrated relative to the lattice O 1s, taken to be at 529.83 eV.

	CuO	solid solutions[a]	literature[b]
Cu^{2+} $2p_{3/2}$ peak 1	933.06	932.34-933.45	933.51-933.6
Cu^{2+} $2p_{3/2}$ peak 2	934.71	934.52-935.35	933.74-933.8
Cu^{2+} $2p_{3/2}$ satellite 1	941.42	938.94-941.48	
Cu^{2+} $2p_{3/2}$ satellite 2	943.80	942.39-943.94	
Cu^{2+} $2p_{1/2}$ peak 1'	952.65	952.65-953.53	953.45
Cu^{2+} $2p_{1/2}$ peak 2'	954.69	954.44-956.39	
Cu^{2+} $2p_{1/2}$ satellites (not resolved)	961.94	962.03-962.36	
O1s	529.28	529.83	529.31-529.9
Cu L_3VV (as kinetic energy)	918.60	916.90-918.59	917.1-918.6
Cu Auger parameter	1851.66	1849.43-1851.23	1851.7

[a]Solid solution Cu 2p binding energies vary with x, as shown in Figure 3.10.
[b]Literature references taken from refs. [133-136].

III E. Discussion

Solid solutions of copper dissolved into a palladium oxide lattice can be formed homogenously, in single phase up to copper concentrations of approximately $Cu_{0.725}Pd_{0.275}O$. The tetragonal PdO lattice creates a different environment for the Cu^{2+} cation than that found in its stable CuO tenorite crystal structure. Initially the four nearest-neighbor lattice bonds O^{2-} are elongated by about 4% over the tenorite lattice (2.024 *v.s.* 1.95-1.96 Å) and the planar oxygen arrangement, while square planar in pure CuO, is distorted to create $82.5/97.5^0$ angle pairs in PdO. The apical oxygens found at 2.784Å in tenorite have no counterpart in the square planar PdO crystal structure and the new-found environment for Cu^{2+} in this crystal structure can be viewed as an extreme case of Jahn-Teller distortion in which the apical oxygen are completely removed to infinity.

The $Cu_xPd_{1-x}O$ solutions follow Vegard's law over the majority of the single phase concentration range, in which the lattice contracts linearly with copper concentration as the smaller Cu^{2+} replaces Pd^{2+} in the PdO lattice, with the exception of a slight lag for low copper concentrations where the PdO lattice appears to be able to accommodate the smaller Cu^{2+} cation for up to approximately 10% of the total metal content without significant changes from the pure PdO lattice. The initial lag in lattice parameter is not well understood, since there is no apparent bulk phase change in the XRD data, and variation from ideality that result in clustering or other inhomogeneity seem more likely to occur at high concentrations of the solute cation. One possibility is that copper solution into the PdO lattice is initially accompanied by defect formation.

AES intensity quantification of surface composition implies that copper surface depletion might occur for these very low copper concentrations. Surface and bulk concentrations are, otherwise, comparable to within error of the measurement.

Given the extreme elongation of 42% for the apical oxygen in the CuO tenorite structure, it is perhaps not surprising that the square planar coordination results in similar Cu 2p peak shapes and satellite structure. The peak structure has been analyzed in a number of studies[109,118-126] and the relative intensities and peak shapes of the individual components used to model the peak structure (Figure 3.8) have been described in terms of hybridization with the O 2p levels, which leads to screened, main-peak states (A+B) which share copper photoemission "hole" density with the surrounding oxygen ligands and unscreened satellite states resulting in peaks C+D. Initially at low copper concentration, the intensity of copper photoemission from unscreened states is higher in the $Cu_xPd_{1-x}O$ solid solution than in pure tenorite, but as copper content increases and the Cu-O distances become comparable the relative intensities approach that observed in tenorite. The presence of the apical oxygen appears to have very little effect on the copper photoemission, with hybridization largely controlled by overlap with planar oxygen.

The peak width of the main Cu 2p feature has also been associated with CuO structural variation. Copper oxide thin crystalline films grown atop $SrTiO_3$[121] showed a tetragonal CuO unit cell, which produced a broadened Cu 2p peak shape relative to that found for monoclinic CuO (tenorite). The broadening was reported to be due to the change in relative component intensities I_A/I_B and I_C/I_D. The $SrTiO_3$-templated tetragonal CuO system is quite different than the present $Cu_xPd_{1-x}O$ solid solutions, with the former

formed as a 4-5 layer thin film forced into a highly strained structure by the templating $SrTiO_3$ substrate, but which retains similar Cu-O bonding distances to the CuO tenorite structure. In the $Cu_xPd_{1-x}O$ solid solutions, the Cu-O distance varies with copper concentration, and the binding energies of the component vary accordingly. In the present study, the relative intensities I_A/I_B and I_C/I_D remain constant to within the error of the measurement, regardless of c/a lattice parameter ratio or the distortion from the ideal 90^0 planar Cu-O bonding arrangement. Rather, a significant shift in binding energy occurs with copper concentration within the solid solutions, with peak A shifting to higher values, whereas peak B shifts slightly to lower values, resulting in a narrowing of the compound (A+B) main peak.

Binding energy shifts that occur for both Pd^{2+} and Cu^{2+} components of the solid solutions appear to be due primarily to an increase in Madelung energy with copper concentration as the lattice contracts upon substitution of Pd^{2+} with the smaller Cu^{2+} cation and to relaxation effects that occur due to ligand polarization during photoemission in response to the creation of the core hole. Both Pd 3d and Cu 2p binding energies show substantial shifts of approximately 1 eV over the range of the solid solution, $0 \leq x \leq 0.725$ for $Cu_xPd_{1-x}O$. In the absence of final state screening, operant for the Pd 3d peaks and the C and D components of the Cu 2p satellites, the individual components all shift to higher binding energy. For the main Cu 2p peak, which results from non-local (peak A) and local (peak B) O 2p screened final states, only the local peak does not shift to higher binding energies, but shows a slight negative shift with increasing copper concentration. While screening lowers the binding energy relative to the unscreened final state through both local and nonlocal mechanisms, local screening which places a hole on the

surrounding nearest-neighbor oxygen ligand suffers from repulsive interactions with the core copper 2p hole that are ameliorated by delocalization of the O 2p hole.[119] The hole-hole repulsion will only be intensified as increased copper concentration results in a decrease in Cu-O bonding distance.

III F. Conclusions

$Cu_xPd_{1-x}O$ has been synthesized as single-phase, homogeneous solid solutions over a wide range of $0 \leq x \leq 0.725$ and, with the exception of a small, low-concentration lag follow Vegard's law over the range of homogeneity. While individual unit cell parameters decrease linearly as Cu^{2+} is substituted for the larger Pd^{2+} cation, the c/a ratio increases, decreasing the distortion from 90^o found in the square planar PdO crystal structure. The copper environment differs from that of CuO tenorite, initially at low x-values having longer bonding distances and with no apical oxygen coordinating the copper cation. However, the peak structure found for the Cu 2p XPS spectra remains relatively constant, indicating that the planar oxygen coordination is most influential in controlling hybridization effects that contribute to the satellite structure. Both copper and palladium core XPS peaks shift to higher binding energies with increased copper content, which can be explained by increased Madelung energies and relaxation effects that occur with decreased Cu-O bonding distance.

Acknowledgement

We gratefully acknowledge support from the National Science Foundation (NSF CHE-1012366).

References

[66] Christensen, G. L., Langell, M. A., J. Phys. Chem. C, **2013**, 117 (14), pp 7039–7049

[67] Réti, F.; Kiss, G.;Perczel, I. V. *Sensor Mater*. **2004**, *16(2)*, 53-69.

[68] Dobos, K.; Zimmer, G. *IEEE Trans. Electron Devices* **1985**, *32(7)*, 1165- 1169.

[69] Seal, S.; Shukla, S. *JOM* **2002**, *54(9)*, 35-38.

[70] Kaneko, H.; Okamura, T.; Taimatsu, H.; Matsuki, Y.; Nishida, H. *Sens. Actuators, B* **2005**, *108*, 331-334.

[71] Kim, J. Il.; Han, S. D.; Singh, I.; Lee, H. D.; Wang, J. S. *Sens. Actuators B* **2005**, *107*, 825-830.

[72] Vrňata, M.; Myslík, V.; Vysloužil, F.; Jelínek, M.; Lančok, J.; Zemek, J. *Sens. Actuators B* **2000**, *71*, 24-30.

[73] Shen, Y.; Yamazaki, T.; Liu, Z.; Meng, D.; Kikuta, T.; Nakatani, N.; Saito, M.; Mori, M. *Sens. Actuators, B* **2009**, *135*, 524-529.

[74] Yuasa, M.; Masaki, T.; Kida, T.; Shimanoe, K.; Yamazoe, N. *Sens. Actuators B* **2009**, *136*, 99-104.

[75] Salker, A. V.; Choi, N. J.; Kwak, J. H.; Joo, B. S.; Lee, D. D. *Sens. Actuators*, B **2005**, *106*, 461-467.

[76] Wang, X.; Hui, C.; Liu, H.; Du, G. J.; He, X. S.; Xi. Y. *Sens. Actuators* B **2010**, *144*, 220-225.

[77] De, G.; Licciulli, A.; Massaro, C.; Quirini, A.; Rella, A.; Siciliano, P.; Vasanelli, L. *Sens. Actuators* B **1999**, *55*, 134-139.

[78]Nguyen, D. H.; El-Saffy, S. A. *Anal Methods*, **2011**, *3(9)*, 1948-1956.

[79] Gou, X.; Wang, G.; Yang, J.; Park, J.; Wexler, D. *J. Mater. Chem.* **2008**, *18*, 965-969.

[80]Kung, H. H, *Transition Metal Oxides: Surface Chemistry and Catalysis; Stud. Surf. Sci. Catal.,* vol. 45, Elsevier Science Publishers B.V. Amsterdam, The Netherlands, 1989.

[81] Van Giezen, J. C.; Van Den Berg, F. R.; Kleinen, J. L.; Van Dillen, A. J.; Geus, J. W. *Catal. Today* **1999**, 47, 287-293.

[82] Lenihan, S.; Curtin, T. *Catal. Today* **2009**, *145(1-2)*, 85-89.

[83] Fox, E. B.; Lee, A. F.; Wilson, K.; Song, C. *Top. Catal.* **2008**, *49*, 89-96.

[84] Scotti, N.; Monticelli, D.; Zaccheria, F. *Inorg. Chem. Acta* **2012**, *380*, 194-200.

[85] Mowery, D. L.; Graboski, M. S.; Ohno, T. R.; McCormick, R. L. *Appl. Catal., B* **1999**, *21*, 157-169.

[86] Wachs, I. E.; Routray, K. *ACS Catalysis* **2012**, *2(6)*, 1235-1246.

[87] Kulkarni, D.; Wach, I. E. *Appl. Catal. A* **2002**, *273*, 121-137.

[88] Schuyten, S.; Dinka, P.; Mukasyan, A. S.; Wolf, E. *Catal. Lett.* **2008**, *121(3-4)*, 189-198.

[89] Weaver, J. F.; Devarajan, S. P.; Can, H. *J. Phys. Chem. C* **2009**, *113(22)*, 9773-9782.

[90] Liu, J.; Huang, X.; Li, Y.; Sulieman, K. M.; He, X.; Sun, F. *J. Mater. Chem.*, **2006**, *16(45)*, 4427-4434.

[91] Rogers, D. B.; Shannon, R. D.; Gillson, J. L. *J. Solid State Chem.* **1971,** *3(2)*, 313-316.

[92] Park, K. T.; Novikov, D. L.; Gubanov, V. A.; Freeman, A. J. *Phys. Rev. B* **1994,** 49 *(7)*, 4425-4431.

[93] Wold, A.; Dwight, K. *Solid State Chemistry Synthesis, Structure, and Properties of Selected Oxides*; Chapman & Hall, Inc.,: New York, NY, **1993**; p 94.

[94] Lide, D. R., Ed. *CRC Handbook of Chemistry and Physics, 91st ed.*; Taylor & Francis Group: Boca Raton, FL, **2010**, pp 11-12.

[95] Schmahl, N. G.;Eikerling, G. F. *Zeit. Phys. Chem.* **1968**, *62(5)*, 268-279.

[96] Lide, D. R., Ed. *CRC Handbook of Chemistry and Physics*; Taylor & Francis Group: Boca Raton, FL, **2010**; pp 4- 79.

[97] XPSPeak4.1 is a freeware fitting program developed by Kwok, R.;

http://www.phy.cuhk.edu.hk/~surface/download.html

[98] Shirley, D.A. *Phys. Rev., B* **1972**, *55(12)*, 4709-4714.

[99] Vegh, J. *J. Electron Spectrosc. Rel. Phenom.* **2006**, *151(3)*, 159-164.

[100] Denton, A. R.; Ashcroft, N. W. *Phys. Rev. A* **1991**, *43(6)*, 3161-3164.

[101] Mroczkowski, S.; Lichtman, D. *J. Vac. Sci. Technol. A* **1985**, *3(4)*, 1860-1865.

[102] Wagner, C. D.; Riggs, W. M.; Davis, L. E.; Moulder, J. F.; Mullenberg G. E. Ed. *Handbook of X-Ray Photoelectron Spectroscopy*, Perkin-Elmer Physical Electronics Division: Eden Prairie, MN, **1978**, p. 188.

[103] Wagner, C. D.; Riggs, W. M.; Davis, L. E.; Moulder, J. F.; Mullenberg G. E. Ed. *Handbook of X-Ray Photoelectron Spectroscopy*, Perkin-Elmer Physical Electronics Division: Eden Prairie, MN, **1978**, pp 110-111**.**

[104] Gabasch, H.; Hayek, K.; Klötzer, B.; Unterberger, W.; Kleimenov, E.; Teschner, D.; Zafeiratos, S.; Hävecker, M.; Knop-Gericke, A.; Schlögl, *et al. J. Phys. Chem. C* **2007**, *111(22)*, 7957- 7962.

[105] Moddeman, W. E.; Bowling, W. C.; Carter, D. C.; Grove, D. R. *Surf. Interface Anal.* **1988**, *11(6-7)*, 317-326.

[106] Légaré, P.; Finck, F.; Roche, R.; Maire, G.; *Surf. Sci.* **1989**, *217(1–2)*, 167-178.

[107] Kim, K. S.; Gossmann, A. F.; Winograd, N. *Anal. Chem.* **1974**, *46 (2)*, 197-200.

[108] Brun, M.; Berthet, A.; Bertolini, J. C. *J. Electron. Spectrosc. Relat. Phenom.* **1999**, *104*, 55-60.

[109] Wang, J.; Yun Y.; Altman, E.I.; *Surf. Sci.* **2007**, *601*, 3497-3505.

[110] Gaskell, K. J.; Starace, A.; Langell, M. A. *J. Phys. Chem. C* **2007**, 111, 13912-13921.

[111] Biesinger, M. C.; Payne, B. P.; Grosvenor, A. P.; Lau, L. W. M.; Gerson, A. R.; Smart, R. St. C. *Appl. Surf. Sci.* **2010**, *257(7)*, 2717-2730.

[112] Cox, P. A. *Transition Metal Oxides: An Introduction to Their Electronic Structure and Properties*; Oxford University Press: New York, NY, **1992**.

[113] Pillo, Th.; Zimmermann, R.; Steiner, P.; Hüfner, S. *J. Phys.: Condens. Matter* **1997**, *9*, 3987-3999.

[114] Hass K.C.; Carlsson, A.E. *Phys. Rev. B*, **1993**, 46 (7), 4246-4249.

[115] Briggs, D.; Seah, M. P. *Practical Surface Analysis, Auger and X-ray Photoelectron Spectroscopy, Vol. 1, 2nd ed.*; John Wiley and Sons: New York, NY, **1988**, 543-544.

[116] Van der Heide, P. A. W. *J. Electron Spectrosc. Rel. Phenom.* **2008**, *164*, 8-18.

[117] Shen, Z. X.; List, R. S.; Dessau, D. S.; Parmigiani, F.; Arko, A. J.; Bartlett, R.; Wells, B. O.; Lindau I.; Spicer, W. E. *Phys. Rev. B.* **1990**, *42(13)*, 8081-8085.

[118] Fetisov, A.; Kuznetsov *J. Appl. Spectrosc.* **2009**, *76(4)*, 523-527.

[119] Van Veenendaal, M. A.; Eskes, H.; Sawatzky, G. A. *Phys. Rev. B* **1993**, 47(17), 11462.

[120] Eskes, H.; Tjeng, L. H.; Sawatzky, G. A. *Phys. Rev. B* **1990,** 41(1), 288.

[121] Siemons, W.; Koster, G.; Blank, D. H.; Hammond, R. H.; Geballe, T. H.; Beasley, M. R. *Phys. Rev. B* **2009**, *79*, 195122/1-7.

[122] Galakhov, V. R.; Finkelstein, L. D.; Zatsepin, D. A.; Kurmaev, E. Z.; Samokhvalov, A. A.; Naumaov, S. V.; Tatarinova, g. K.; Demeter, M.; Bartkowski, S.; Neumann, M.; Moewes, A. *Phys. Rev. B* **2000**, *62(8)*, 4922-4926.

[123] Gupta, R. P; Sen, S. K., *Phys. Rev. B* **1975**. 12(1) 15.

[124] Grosvenor, A. P.; Biesinger, M. C. St.C. Smart, R.; McIntyre, N. S., *Surf. Sci.* **2006**, 600, 1771.

[125] Soriano, L.; Preda, I.; Gutierrez, A.; Palacin, S.; Abbate, M.; Vollmer, A. *Phys. Rev. B.* **2007**, 75, 233417.

[126] Ghijsen, J.; Tjeng, L. H.; van Elp, J.; Eskes, H.; Westerink, J.; Sawatsky, G. A.; Czyzyk, M. T., *Phys. Rev. B,* **1988**, 38, 11322.

[127] Bagus, P. S.; Illas, F.; Pacchioni, G.; Parmigiani, F., *J. Electron Spectrosc. Rel. Phenom.*, **1999**, 100, 215.

[128] Guittet, M. J.; Crocombette, J. P.; Gautier-Soyer, M., *Phys. Rev. B,* **2001**, 63, 125117.

[129] Cole, R. J.; Gregory, A. C.; Weightman, P., *Phys. Rev. B,* **1994**, 49, 5657.

[130] Wagner, C. D. *Anal. Chem.* **1972**, 44, 967.

[131] Moretti, G. *J. Electron Spectrosc. Rel. Phenom.* **1998**, 95(2-3), 95.

[132] Dupin, J.-C.; Gonbeau, D.; Vinatier, P.; Levasseur, A. *Phys. Chem. Chem. Phys.*, **2000**, *2*, 1319-1324.

[133] Sarkar, S.; Jana, P. K.; Chaudhuri, B.K. *Appl. Phys. Lett.* **2006**, 89 212905-1/3.

[134] Wu, C.-K.; Yin, M.; O'Brien, S.; Koberstein, J. T. *Chem. Mater.*, **2006**, *18*, 6054-6058.

[135] Chusuei, C. C.; Brookshier, M. A.; Goodman, D. W. *Langmuir*, **1999**, *15*, 2806-2808.

[136] Tahir, D.; Tougaard, S. *J. Phys.: Condens. Matter*, **2012**, *24*, 175002/1-8.

Chapter 4 - Catalytic Dehydrogenation of Isopropanol

IV A. Abstract

Solid solutions of $Cu_xPd_{1-x}O$ were prepared with x values of 0, 0.2, 0.4, 0.6, and 1. These solid solutions were utilized as catalysts in the dehydrogenation of isopropanol to form acetone. Solid solutions were found to be less efficient catalysts under the anaerobic conditions used when compared to heterogeneous mixtures of equal atomic composition under the same reaction conditions. SEM images were obtained and indicate that the surface morphology changes after the sample is heated. The surface area of the catalysts was determined by BET. UV/VIS was used to determine reactant and product concentrations. XPS data were obtained for the catalysts before and after the reactions, which determined that reduction of the catalyst occurred during catalysis and that palladium segregation to the near-surface region was significant.

IV B. Introduction

Catalysts have dramatically changed our world and made many things possible. This research focuses on the metal oxide catalysts CuO and PdO and the solid solutions thereof for the partial oxidation of alcohols. Dehydrogenation of isopropanol is a reaction of great interest due to industrial demand for acetone production[137,138,139]. Copper oxides are active in partial oxidation catalysis[140] and copper II oxide, in particular, is used as the active catalyst in the dehydrogenation of isopropanol[141,142]. Palladium in its oxidized form is also useful catalyst[143] for the oxidation or partial oxidation of alcohols,[144,145,146,147] although it tends to be somewhat harsher resulting in

total oxidation of some hydrocarbon reactants, thus requiring very precise control of the reaction conditions.

IV C. Experimental

The surface area of each catalyst was determined using a Micromeritics ASAP 2020 Surface Area and Porosity Analyzer Instrument using nitrogen as the adsorptive gas and held at liquid nitrogen temperature. SEM images were also taken and reveal surface morphology of the as-purchased PdO and CuO before and after heating, along with some solid solution samples. Heterogeneous catalysis was carried out in the liquid phase using isopropanol as the liquid phase. Setup consisted of a 500ml three-neck round bottom flask equipped with a large condensing column on the center neck. A volume of 250ml of isopropanol was poured into the flask and heated to boiling with stirring. The other necks were capped with septums. Once the normal boiling temperature of acetone, 56^0C, was achieved, one septum was removed and about 0.2g of catalyst powder was added to the flask, taken to be time zero, by means of a scoopula and the neck was immediately capped with a septum. Hydrogen was allowed to escape through the top of the condensing column. Samples of the liquid phase were taken by syringe beginning at 30 minutes and then every hour for the first ten hours. Then a sample was taken at about 24hrs and intermittently until the reaction was stopped. Reactant and product composition of the liquid-phase samples were determined with UV/VIS spectroscopy on a Shimadzu UV-2401 PC UV-VIS Recording Spectrometer. Standard samples of the liquid phase were prepared with acetone concentrations in isopropanol varying in increments of 0.05% from 0 to 2% acetone concentrations by volume. The absorbance of each standard sample was measured and plotted. This produced a linear plot from which

an equation was generated that could be used to determine the concentration of acetone in a sample in the reaction mixture.

Acetone has a high molar absorptivity[148] of 13.9 L/mol*cm at 280 nm, making UV/VIS a very sensitive method for its detection[149]. The presence of isopropanol and acetone were also confirmed by NMR using a BrukerAdvance III-HD 400 Mhz NMR. Stopping the reaction consisted of turning off the heat and allowing the reaction flask to cool while stirring. Once cooled to room temperature the reaction mixture was vacuum filtered. The solid catalyst was recovered and analyzed by x-ray photoelectron spectroscopy to identify changes that occurred on the catalyst surface during catalysis.

Results

BET surface area analysis results, given in tables 4.1 and 4.2, indicate that the catalysts have moderately low surface area, as expected because the synthetic procedure was not optimized for surface area. Surface areas of heterogeneous mixtures of CuO/PdO, used for comparison to solid solution activity, were estimated from the average surface areas of the pure metal oxides that have undergone the same heating process used to synthesize the solid solutions.

A representative isotherm of the solid-solution $Cu_{0.40}Pd_{0.60}O$ is shown in Figure 4.1. The first plateau is the region where one monolayer of N_2 has been absorbed on the sample surface. Figure 4.2 is an expansion of the plot in the region that indicates a complete monolayer of N_2 has been formed. A complete monolayer is all that is needed in order to determine the surface area of the sample if it is assumed that the first monolayer forms completely before the beginning of adsorption of the second layer. The surface area is then estimated by the area of the adsorbed nitrogen molecule multiplied by

the amount of nitrogen adsorbed in the monolayer. The best linear fit to this region results in a y-intercept that is equal to the quantity of N_2 absorbed when then monolayer is complete. This information is used to calculate the surface of the sample.

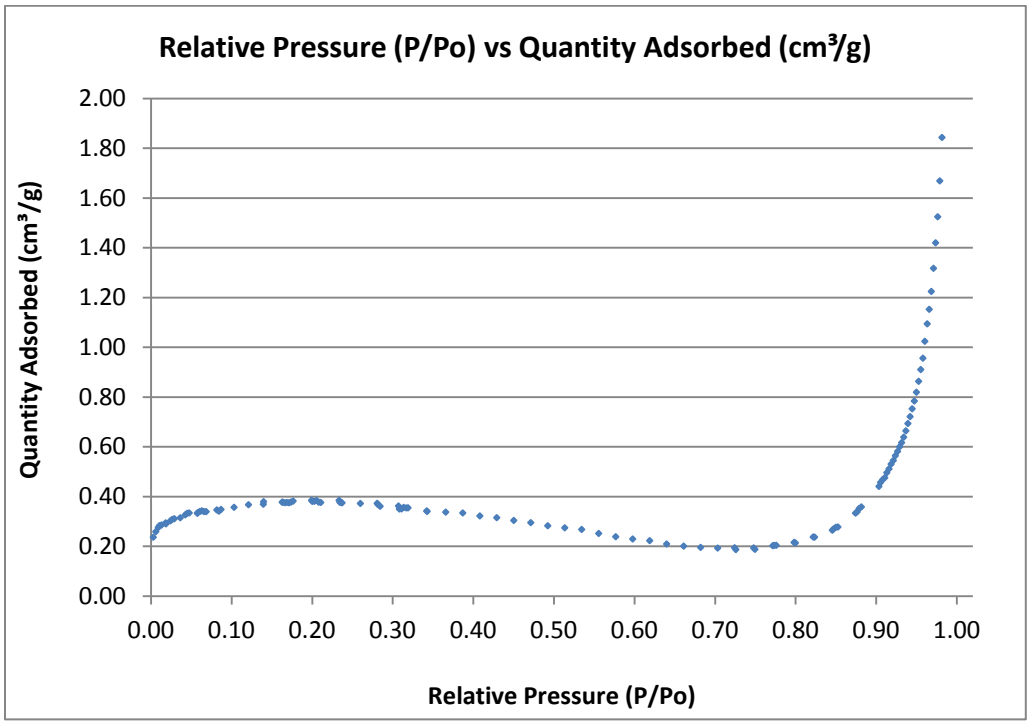

Figure 4.1 Representative BET isotherm of $Cu_{0.40}Pd_{0.60}O$ demonstrating the relative pressure vs. the quantity absorbed. The first plateau is the region where one monolayer of N_2 has been absorbed on the sample surface.

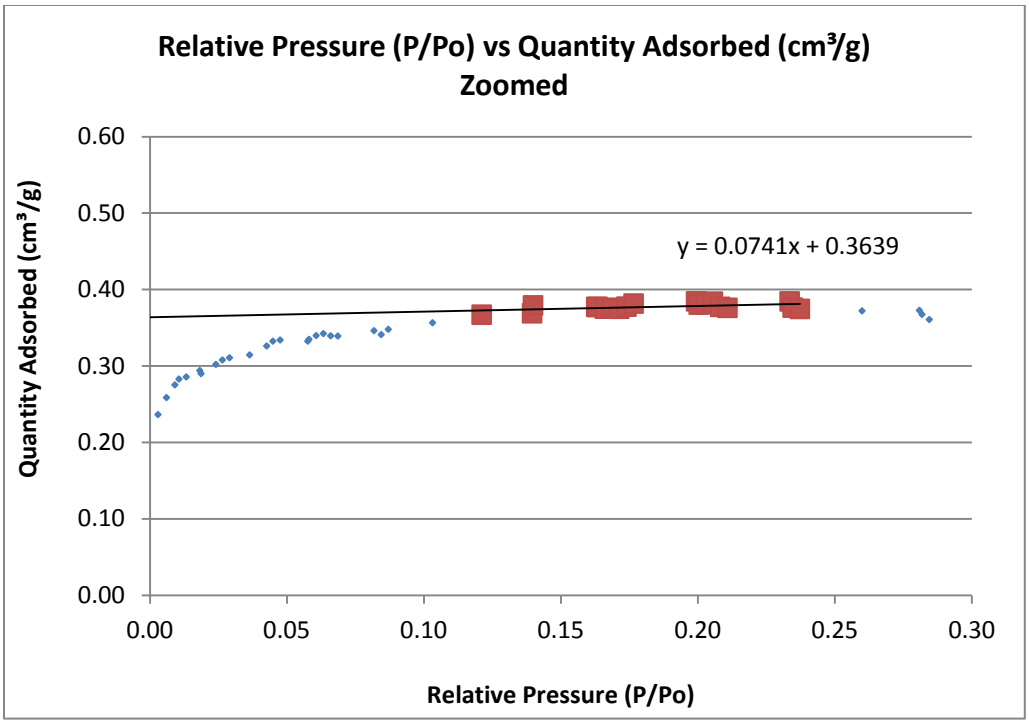

Figure 4.2 Expanded BET isotherm of $Cu_{0.40}Pd_{0.60}O$ with best fit line of monolayer plateau region.

According to the BET measurements, results for which are given in table 4.1, the solid solution samples have a larger surface area than the pure PdO or CuO, yet as observed in figure 4.7 CuO produced the most acetone per unit surface area for a given reaction time. PdO produced the least amount of acetone. The heterogeneous samples also has much smaller surface areas according to table 4.1 and 4.2 since they were averaged values of the composite pure metal monoxides.

Sample	Sample Size (g)	Quantity Adsorbed when monolayer is complete (cm^3/g)	**Surface Area (m^2/g)** (Calculated from monolayer)
Heated PdO	0.6665	0.1420	**0.7650**
$Cu_{0.20}Pd_{0.80}O$	0.3228	0.4000	**2.1550**
$Cu_{0.40}Pd_{0.60}O$	0.3419	0.3639	**1.9605**
$Cu_{0.60}Pd_{0.40}O$	0.1415	0.1578	**0.8501**
Heated CuO	4.7976	0.0573	**0.3087**

Table 4.1 Surface area the solid solution samples and heated CuO and PdO.

Sample	**Non Solid Solution** (Estimated from heated PdO and CuO measurements) **Surface Area (m2/g)**
$Cu_{0.20}Pd_{0.80}O$	**0.6738**
$Cu_{0.40}Pd_{0.60}O$	**0.5825**
$Cu_{0.60}Pd_{0.40}O$	**0.4912**

Table 4.2 Estimated Surface area of heterogeneous mixture samples.

SEM images of select samples were taken in order to understand the surface morphology changes that occur upon heating. It is expected that heating CuO and PdO to high temperatures would decrease the surface area and indications of this are observed in figures 4.3 and 4.4. CuO as purchased has a very interesting morphology which after the heating cycle changes dramatically to a smoother stacked structure. PdO as purchased has a slightly porous structure which upon heating changes to a very non-porous surface. Two solid solution sample SEM images are observed in figure 4.5. These samples resemble the heated CuO and PdO samples. Heating in sample synthesis is, therefore, one significant factor in the low surface areas obtained, and synthesis by alternative methods instead of thermal diffusion might be considered if high-surface area particles are desired.

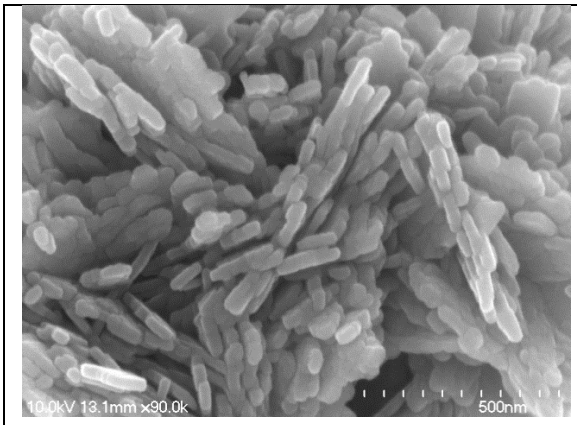

CuO Unheated - as purchased

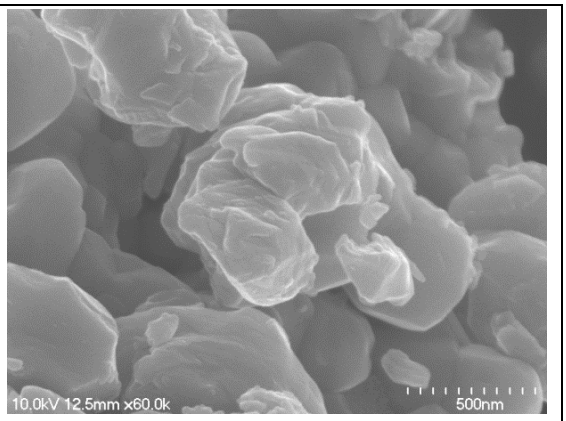

CuO Heated

Figure 4.3 SEM images of as purchased CuO and CuO that has been heated showing the change in surface area and morphology when CuO is heated.

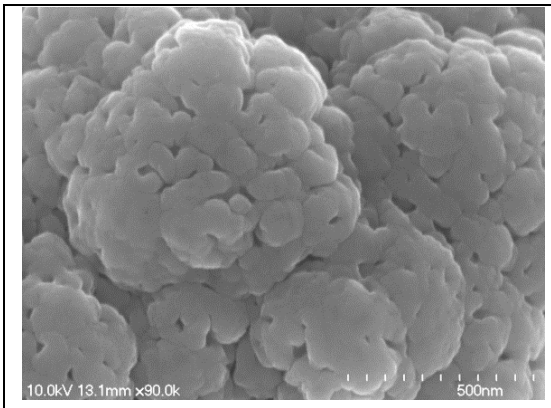

PdO Unheated - as purchased

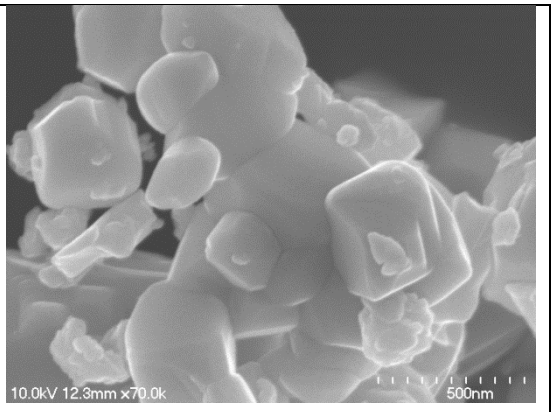

PdO Heated

Figure 4.4 SEM images of as purchased PdO and PdO that has been heated. The surface appears to be less porous and smoother after heating.

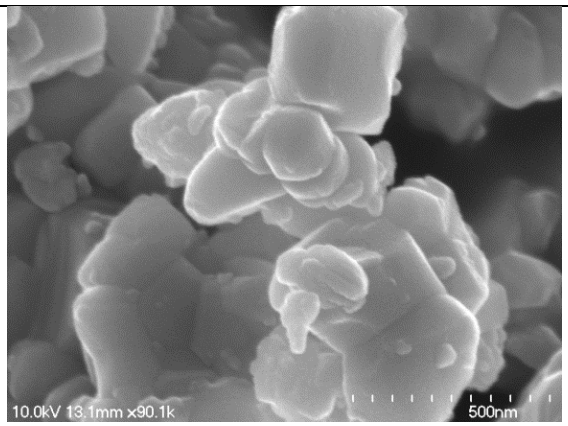

$Cu_{0.10}Pd_{0.90}O$

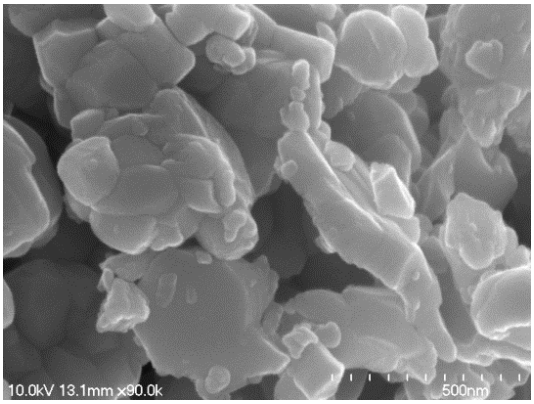

$Cu_{0.40}Pd_{0.60}O$

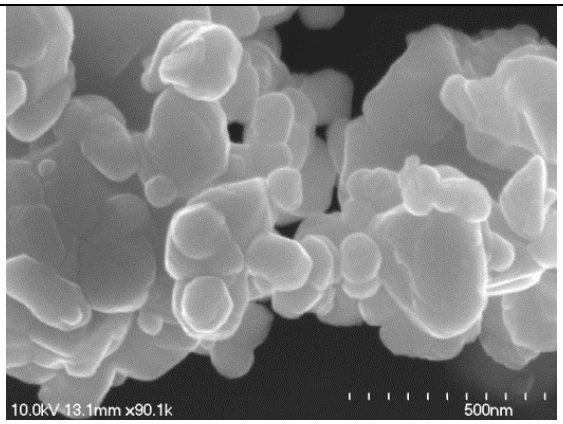

$Cu_{0.70}Pd_{0.30}O$

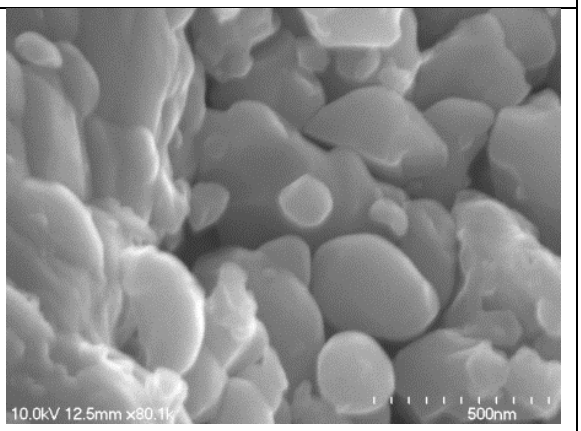

$Cu_{0.80}Pd_{0.20}O$

Figure 4.5 SEM images of solid solution samples. These samples somewhat resemble the heated CuO and PdO samples.

The most likely reaction mechanism for isopropanol to acetone production catalyzed by oxide surfaces[150,151] is in equation 1.

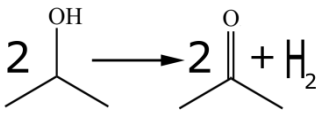

(1)

This reaction is endothermic and requires heat input. Another mechanism that has also been proposed is exothermic and is in equation 2.

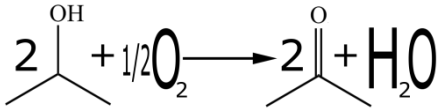

(2)

and requires temperature control. A competing reaction in which the oxygen is completely removed from the isopropanol molecule to produce propene has also been observed [150], but this a minor by-product which can be controlled through the use of selective catalysts. Figure 4.6 illustrates a possible mechanism[152,153,154,155] as to how the catalyst surface participates in the conversion of isopropanol to acetone. The first step is the attraction of the hydrogen atom on the hydroxyl group to an oxygen atom in the metal oxide. The hydrogen atom is then removed from isopropanol as the hydrogen stays with the oxide and the hydroxyl oxygen is attracted to one of the metals from the oxide. The next step is for another oxide oxygen atom to attract to the hydrogen atom on the same carbon atom. The final step for the removal of that second hydrogen atom. The newly formed acetone molecule is free to leave, and the two hydrogen atoms on the oxide surface may now combine to form hydrogen gas.

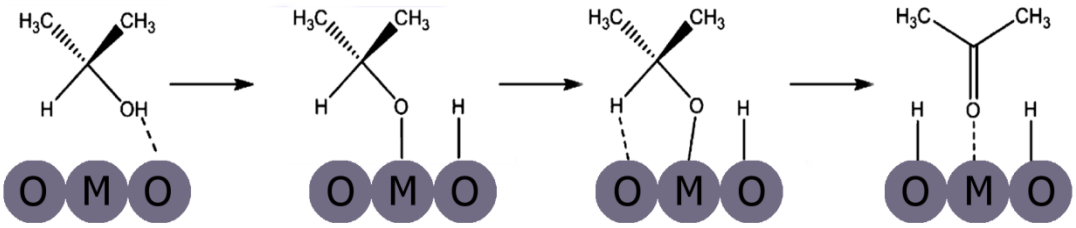

Figure 4.6 Possible mechanism for conversion of isopropanol to acetone on the surface of a metal oxide catalyst. The labels M and O are for metal and oxygen respectively.

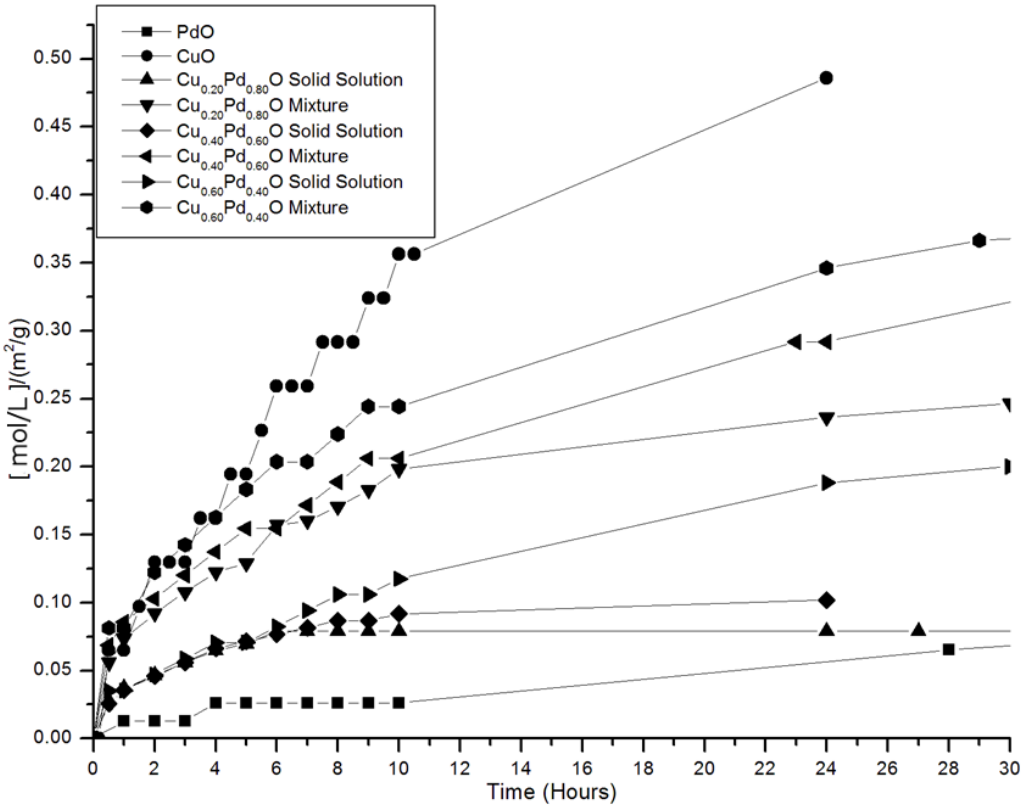

Figure 4.7 Time vs. (mol/L)/(m^2/g).

Figure 4.7 shows acetone production catalyzed by the oxide surfaces over time. The y-axis of figure 4.7 shows that the concentration of acetone was divided by the surface area of the catalyst to correct for variations in surface area. This surface area adjustment allows us to focus on catalyst performance based on the other catalyst properties such as elements present and their concentrations. It is apparent that CuO outperforms PdO. In both the solid solutions and the non-solid solution mixture we see that the acetone production increases as the Cu concentration is increased. An interesting observation is that all of the heterogeneous solution mixtures outperform the solid solution counterparts. Perhaps this is because the solid solutions have the PdO unit cell structure which must not perform as well as the CuO lattice structure due to oxygen transport problems.

However, the segregation of palladium during catalysis must also be taken into account, and the solid solutions in part deactivate as the surface becomes enriched in palladium. Even the heterogeneous mixture with only 20% Cu outperforms the solid solution with 60% Cu.

	Pure PdO	Pure PdO (Used as Catalyst)	Solid Solution	Solid Solution (Used as Catalyst)
Pd^{2+} $3d_{5/2}$	336.43	334.57	336.51-337.23	333.57-334.23
Pd^{2+} $3d_{3/2}$	341.70	339.79	342.53-341.83	338.79-339.42
O 1s lattice	529.83	531.31	529.83	531.76-532.29
Pd $M_{4,5}N_{2,3}V$ (as kinetic energy)	273.0	262.16	273.0	265.49-261.09
α_1 (Auger parameter 1)	609.4	596.73	609.7	595.32-599.06
Pd M_5VV (as kinetic energy)	327.1	331.3	327.2	331.62-330.19
α_2 (Auger parameter 2)	663.5	665.87	663.8	663.87-665.85

Table 4.3 Pd XPS data in eV, Intensity was too low to identify any satellite peaks.

	Pure CuO	Pure CuO (Used as Catalyst)	Solid Solutions*	Solid Solution (Used as Catalyst)
Cu^{2+} $2p_{3/2}$ peak 1	933.06	934.05	932.34-933.45	930.23-930.69
Cu^{2+} $2p_{3/2}$ peak 2	934.71		934.52-935.35	
Cu^{2+} $2p_{1/2}$ peak 1'	952.65	954.09	952.65-953.53	950.27-950.40
Cu^{2+} $2p_{1/2}$ peak 2'	954.69		954.44-956.39	
O1s	529.28	529.45	529.83	531.76-532.29
Cu L_3VV (as kinetic energy)	918.60	917.32	916.90-918.59	920.63-920.62
Cu Auger parameter	1851.66	1851.40	1849.43-1851.23	1850.90-1851.30

Table 4.4 Cu XPS data in eV; Cu^{2+} $2p_{3/2}$ peak 1 was not resolved from Cu^{2+} $2p_{3/2}$ peak 2 and Cu^{2+} $2p_{1/2}$ peak 1' was not resolved from Cu^{2+} $2p_{1/2}$ peak 2'.

Tables 4.3 and 4.4 contain XPS data for some of the catalysts before and after use. There are noticeable peak shifts observed. The Pd^{2+} $3d_{5/2}$ and the Pd^{2+} $3d_{3/2}$ peaks for both the pure PdO and the solid solutions shifted to lower binding energy indicating reduction while the O 1s shifted higher. The Pd $M_{4,5}N_{2,3}V$ and α_1 (Auger parameter 1) shifted lower for both PdO and the solid solutions while the Pd M_5VV and α_2 (Auger parameter 2) shifted higher. In chapter 3 it was noted that there was not a consistent trend for the Pd Auger transitions and that seems to apply here as well. The Auger parameter was given as equation 5 in chapter 3 and is labeled listed in tables 4.3 and 4.4. The CuO sample did not change significantly after use as a catalyst indicating a more robust catalyst for the selected reaction possibly due to its ability to transport oxygen to the surface region. The solid solutions however, did show some peak shifts and may help explain why the heterogeneous samples outperformed the solid solution samples. The solid solutions had the Cu^{2+} $2p_{3/2}$ peak 1, Cu^{2+} $2p_{3/2}$ peak 2, Cu^{2+} $2p_{1/2}$ peak 1', and the

Cu^{2+} $2p_{1/2}$ peak 2' shift lower indicating reduction. The O 1s, Cu L_3VV and the Cu Auger parameter shifted higher. The Cu Auger parameter is still very similar to that of the solid solutions before being used as a catalyst. The slight increase may be due to the shift in copper concentration that occurred as well as the sample reduction that was observed.

XPS of the catalysts after use was performed, but was more challenging to obtain good intensities for the copper component. $Cu_{0.20}Pd_{0.80}O$ initially had a Cu concentration of 20.4% and a Pd concentration of 79.6%, but no peaks for Cu were present after use as a catalyst. It is noted that in table 4.5 the surface oxygen concentration increased dramatically. This is likely due either acetone or isopropanol remaining on the sample. It was expected that the oxygen concentration of the samples would decrease as that would be consistent with catalyst reduction.

The Pd and Cu concentrations were compared for the two remaining catalysts and revealed conflicting results. The Cu concentration decreased for $Cu_{0.40}Pd_{0.60}O$, but increased for $Cu_{0.60}Pd_{0.40}O$. This phenomenon is hard to explain and would require further investigation.

	Surface Oxygen Concentration Before Catalysis	Surface Oxygen Concentration After Catalysis
CuO	60.2%	82.3%
PdO	76.0%	98.4%

Table 4.5 Surface Oxygen concentration before and after use as a catalyst as determined by XPS.

	Surface Palladium Concentration Before Catalysis	Surface Palladium Concentration After Catalysis	Surface Copper Concentration Before Catalysis	Surface Copper Concentration After Catalysis
$Cu_{0.40}Pd_{0.60}O$	61.1%	78.2%	38.9%	21.8%
$Cu_{0.60}Pd_{0.40}O$	44.0%	38.6%	56.0%	61.4%

Table 4.6 Comparison of Palladium and Copper Concentration before and after use as a catalyst determined by XPS.

IV D. Conclusion

Solid Solutions have been prepared and compared to heterogeneous samples of equal atomic compositions for the production of acetone from isopropanol. While all samples were capable of producing acetone under the given conditions, samples were easily distinguished by their results. It is clear that CuO outperformed PdO and that both the heterogeneous and solid solution catalysts increased in performance with increasing CuO. Solid solutions did not perform as well as their heterogeneous counterparts.

References

[137] Badri, N., Chhiti, Y., Bentiss, F., Bensitel, M., Propan-2-ol (Isopropanol) conversion to propene and acetone over V_2O_5 catalysts supported on activated carbon (AC), The second International conference on smart applications and data analysis for smart cities, February **2018.**

[138] Tan, S. T., Umar, A. A., Selleh, M. M., Synthesis of defect-rich, (001) faceted-ZnO on a FTO substrate as efficient photocatalysts for dehydrogentation of isopropanol to acetone, Journal of Physics and Chemistry of Solids **2016,** 93, 73-78.

[139] Mert, M. S., Salt, I., Karaca, F., Mert, H. H., Bolat, E., Multiple Regression analysis of catalytic dehydrogentation of isopropanol in a chemical heat pump system, Chem. Eng. Technol. **2015**, 38(3), 399-408.

[140] Espinós, J. P., Morales, J., Barranco, A., Caballero, A., Holgado, J. P., and González-Elipe, A. R., Interface Effects for Cu, CuO, and Cu_2O Deposited on SiO_2 and ZrO_2. XPS Determination of the Valence State of Copper in Cu/SiO_2 and Cu/ZrO_2 Catalysts. J. Phys. Chem. B **2002**, 106, 6921-6929.

[141] Bálsamo, N. F., Chanquía, C. M., Herrero, E. R., Casuscelli, S. G., Crivello, M. E., Eimer, G. A., Dehydrogentation of Isopropanol on Copper-Containing Mesoporous Catalysts, Ind. Eng. Chem. Res. **2010**, 49, 12365-12370.

[142] Kvande, I., Chen, D., Ronning, M., Venvik, H. J., Holmen, A., Highly Active Cu-based catalysts on carbon nanofibers for isopropanol dehydrogenation, Catalysis today, **2005**, 100, 391-395.

[143] Dianat, A., Seriani, N., Bobeth, M., Pompe, W., Ciacchi, L. C., DFT Study of the Thermodynamic Stability of Pd-Pt Bulk Oxide Phases**.** J. Phys. Chem. C **2008**, 112,

13623-13628.

[144] Mallat, T., Baiker, A., Oxidation of Alcohols with Molecular Oxygen on Solid Catalysts, Chem. Rev. **2004**, 104, 3037-3058.

[145] Lee, A. F., Ellis, C. V., Naughton, J. N., Newton, M. A., Parlett, C. M. A., Wilson, K., Reaction-Driven Surface Restructuring and Selectivity Control in Allylic Alcohol Catalytic Aerobic Oxidation over Pd, J. Am. Chem. Soc., **2011**, 133, 5724-5727.

[146] Liotta, L. F., Venezia, A. M., Deganello, G., Longo, A., Martorano, A., Schay, Z., Guczi, L., Liquid Phase Selective Oxidation of Benzyl Alcohol of Pd-Ag Catalyst Supported on Pumice, Catalysis Today **2001**, 66, 271-276.

[147] Cordi, E. M., Falconer, J. L., Oxidation of Volatile Organic Compounds on Al_2O_3, Pd/Al_2O_3 and PdO/Al_2O_3 Catalysts, Journal of Catalysis, **1996**, 162, 104-117.

[148] Feigenbrugel, V., Loew, C., Calvé, S. L., Mirabel, P., Near-UV molar absorptivities of acetone, alachlor, metolachlor, dizinon, and dichlorvos in aqueous solution, Journal of Photochemistry and Photobiology A: Chemistry **2005,** 174, 76-81.

[149] Feigenbrugel, V., loew, C., Calvé, S. L., Mirabel, P., Near-UV molar absorptivities of acetone, alachlor, metolachlor, dizinon, and dichlorvos in aqueous solution, Journal of Photochemistry and Photobiology A: Chemistry **2005,** 174, 76-81.

[150] Lokras, S. S., Deshpande, P. K., Kuloor, N. R., Catalytic dehydrogenation of 2-propanol to acetone, Ind. Eng. Chem. Process Des. Develop., **1970,** 9(2), 293-297.

[151] Rioux, R. M., Vannice, M. A., Hydrogenation/dehydrogenation reactions: isopropanol dehydrogenation over copper catalysts, Journal of Catalysis **2003,** 216, 362-376.

[152] Tan, S., Gray, M. B., Kidder, M. K., Cheng, Y., Daemen, L. L., Lee, D., Lee, H. N., Ma, Y. Z., Doughty, B., Lutterman, D. A., Insight into the Selectivity of Isopropanol

Conversion at Strontium Titanate (100) Surfaces: A Combination Kinetic and Spectroscopic Study, ACS Catal. **2017**, 7, 8118−8129.

[153] Rioux, R.M., Vannice, M. A., Hydrogenation/dehydrogenation reactions: isopropanol dehydrogenation over copper catalysts, Journal of Catalysis **2003,** 216, 362-376.

[154] Kulkarni, D., Wachs, I. E., Isopropanol oxidation by pure metal oxide catalysts: number of active surface sites and turnover frequencies, Applied Catalysis A: General **2002,** 237, 121-137.

[155] Ando, Y., Yamashita, M., Saito, Y., Reaction mechanism of 2-Propanol dehydrogenation with a carbon-supported Ru-Pt composite catalyst in the liquid phase, Bull. Chem. Soc. Jpn., **2003,** 76, 2045-2049.

Chapter 5 - Conclusions and Future Work

It is surprising that the solid solutions showed lower performance than the heterogeneous mixtures in the production of acetone from isopropanol. XPS of the samples after use as a catalyst shows some difference compared to before. This may give us some insight into how metal oxide samples change when used as catalysts. It seems that for the PdO and the solid solutions there was some sample reduction, and this was not noted for the pure CuO. XPS was not done for the heterogeneous samples, but if this trend continued it may explain why the heterogeneous samples outperformed the solid solution samples. A more in-depth XPS study would need to be done in order to verify that this was also the case for the heterogeneous samples. It may be that the CuO in the heterogeneous samples was not reduced as quickly as it was in the solid solutions. When XPS was used to determine atomic percents of oxygen, palladium, and copper, some unexpected results were obtained. If the increased O concentration was due to the presence of acetone or isopropanol then perhaps the samples could be heated some to drive off these residual hydrocarbons in order to get a better idea of the oxygen concentration present on the surface of the catalyst.

Reactions were allowed to continue for at least 24 hours. A further study could be done to determine the catalyst lifetime and also if a catalyst could be regenerated or not. The surface area measurements leave a lot of unanswered questions. While the BET data looks reasonable, the sample size was limited and further investigations could be done to understand why the solid solutions would have larger surface areas than either the CuO or the PdO.

It would be interesting to measure the hydrogen output of the reaction to verify that it agrees with the acetone concentration and with the assumed reaction route for its formation. It would also be interesting to introduce oxygen into the reaction from a source other than the catalyst that has very limited oxygen. With only 0.2 grams catalyst material there is very little oxygen available from the catalyst. This may help since it was noted that the catalyst surface was reduced.

Catalysts of higher surface areas may produce much better acetone yields and synthesis of high surface area samples could be explored in order to understand its role in the chosen reaction.